Citation: Joseph Raj Xavier. Mixed metal nitride-GO nanohybrids reinforced epoxy coatings for improved corrosion protection and mechanical properties in industrial applications. *Journal of Harbin Institute of Technology*(*New Series*). DOI:10.11916/j.issn.1005-9113.2024097

Mixed Metal Nitride-GO Nanohybrids Reinforced Epoxy Coatings for Improved Corrosion Protection and Mechanical Properties in Industrial Applications

Joseph Raj Xavier *

(*Department of Chemistry*, *Saveetha School of Engineering*, *Saveetha Institute of Medical and Technical Sciences*, *Chennai 602105*, *Tamil Nadu*, *India*)

Abstract: Epoxy (EP) coatings were modified with VN, MoN, 2-aminobenzothiazole (ABT), and graphene oxide (GO) to enhance anti-corrosion and mechanical performance. Structural and morphological analysis (SEM/EDX, TEM, TGA, XRD, XPS) confirmed the uniform dispersion of VN/MoN nanoparticles, which significantly improved the barrier properties of the coatings. Electrochemical analysis (scanning electrochemical microscopy (SECM), electrochemical impedance spectroscopy (EIS)) demonstrated superior corrosion resistance for the EP/GO/ABT-VN/MoN coating, with a charge transfer resistance of 1.53×10^{13} Ω · cm^2 and coating resistance of 1.05×0^{13} Ω · cm^2 in 3.5% NaCl solution. SECM measurements showed a 93.5% reduction in electrochemical activity (1.6 nA vs. 24.8 nA for pure epoxy) after 45 d of immersion. The nanocomposite exhibited exceptional adhesion strength (20.3 MPa) and hardness (1382 MPa), with improved hydrophobicity (159° contact angle), effectively preventing corrosive ion penetration. The scientific significance of this study lies in the development of a multifunctional nanocomposite coating that integrates high corrosion resistance, mechanical durability, and hydrophobicity, addressing long-standing challenges in protective coatings for metal structures. The incorporation of GO/ABT-VN/MoN nanoparticles establishes a passive protective layer that not only prevents aggressive ion diffusion but also enhances mechanical strength and interfacial adhesion, ensuring long-term stability. These findings provide a new design strategy for next-generation epoxy-based coatings with superior durability in harsh environments, making them highly relevant for applications in marine, aerospace, and industrial infrastructure.

Keywords: graphene oxide; nanocomposites; coating and corrosion; mechanical properties; functional materials

CLC number: TQ63 **Document code**: A **Article ID**: 1005-9113(2025)00-0000-32

0 Introduction

Steel, known for its strength and versatility, is widely utilized in industries such as petroleum, natural gas, railroads, and infrastructure development due to its machinability and cost-effectiveness[1-2]. However, despite its mechanical advantages, steel is highly susceptible to corrosion when exposed to aggressive environments containing water, chloride ions, and oxygen. Various strategies have been developed to protect steel from corrosion, each with distinct advantages and limitations. Barrier coatings, such as epoxy and polymer films, act by physically shielding the metal from corrosive elements. These coatings are cost-effective and easy to apply, but can deteriorate over time due to mechanical damage or chemical infiltration. Galvanization, which involves coating steel with a layer of zinc, provides sacrificial protection; however, its effectiveness can diminish under harsh environmental conditions. Cathodic protection, employing either sacrificial anodes or impressed current systems, is highly effective for submerged or buried structures but demands complex installation and continuous maintenance. Corrosion inhibitors, often incorporated into concrete or circulating fluids, work by chemically slowing down the corrosion process, though their environmental

Received 2024-10-26.

* Corresponding author.Joseph Raj Xavier,Ph.D, Professor.Email: drjosephrajxavier@ gmail.com.

impact remains a concern[3-5]. In recent years, nanocomposite coatings have emerged as a promising alternative, offering superior barrier performance, enhanced thermal stability, and greater resistance to chemical degradation.

Among organic polymer coatings, epoxy coatings (EPs) have emerged as a preferred choice due to their excellent corrosion resistance, strong adhesion, and mechanical durability[6-10]. However, conventional epoxy coatings suffer from inherent limitations, including microcracks, voids, and vulnerability to the ingress of aggressive ions (O_2, H_2O, Cl^-), which can accelerate corrosion and degrade long-term performance[11-12]. To overcome these limitations, the incorporation of nanomaterials into epoxy matrices has been explored to enhance their barrier, mechanical, and adhesive properties[13-17]. Nanoparticles such as boron nitride (BN), silicon nitride (Si_3N_4), zirconium nitride (ZrN), carbon nitride (C_3N_4), aluminum nitride (AlN), and titanium nitride (TiN) have shown promise as fillers for polymer composites[18-22]. While some of these, such as BN, Si_3N_4, and C_3N_4, are technically non-metal nitrides, they exhibit exceptional chemical stability, thermal conductivity, and hardness, making them highly suitable for anti-corrosion applications. In contrast, transition metal nitrides (TMNs), such as vanadium nitride (VN), hafnium nitride (HfN), molybdenum nitride (MoN), and titanium nitride (TiN), offer metallic conductivity, mechanical strength, and corrosion resistance, and are increasingly being explored for their potential in enhancing the performance of protective coatings[23-27].

Simultaneously, graphene oxide (GO) has been extensively investigated for its outstanding impermeability to gases and liquids, high surface area, and mechanical strength, which contribute to improved anti-corrosion performance in multilayer coatings. Single-layer GO acts as a highly effective barrier by obstructing the diffusion pathways of corrosive agents, while its abundant oxygen-containing functional groups (e. g., hydroxyl, carboxyl, and epoxy groups) promote strong interfacial bonding with epoxy matrices, thereby enhancing the overall corrosion protection performance of the coating[28-31]. Recent studies have shown that combining GO with TMNs, such as GO/VN and GO/BAMS-VN incorporated into polyurethane, can further enhance both the mechanical and corrosion-resistant properties of coatings. Moreover, the surface functionalization of GO with polar groups, such as $-NH_2$, $-SH$, and $-OH$, markedly enhances its compatibility with polymer matrices. This modification minimizes micropore formation and improves the uniformity and protective efficiency of the resulting coating[32-33]. The integration of functionalized organic molecules such as 2-aminobenzothiazole (ABT) has also proven effective in enhancing dispersion, interfacial adhesion, and chemical resistance[34-37]. While both GO and TMNs individually offer excellent corrosion protection due to their barrier effect and intrinsic stability, their combination provides a synergistic advantage. GO delivers impermeability and mechanical reinforcement, while TMNs contribute electrical conductivity, hardness, and electrochemical stability. The hybrid incorporation of these materials improves filler dispersion, enhances interfacial interactions, and delivers multifunctional protection against mechanical stress and electrochemical attack—key attributes for high-performance coatings.

Despite these advancements, the potential of mixed transition metal nitride-based nanocomposites in epoxy coatings remains underexplored[38-40]. This study introduces an innovative strategy to improve the mechanical strength and anti-corrosion performance of epoxy coatings by incorporating GO combined with 2-aminobenzothiazole (ABT)-functionalized VN/MoN nanoparticles. Unlike conventional nanocomposite coatings, this study explores the synergistic effects of GO, ABT, and VN/MoN, which provide multiple protective mechanisms, including enhanced barrier properties, increased adhesion strength, and improved resistance to corrosive electrolytes. The functionalization of VN/MoN with ABT enhances interfacial interactions with the epoxy matrix, thereby minimizing agglomeration and optimizing dispersion within the coating. Electrochemical analyses, including scanning electrochemical microscopy (SECM) and electrochemical impedance spectroscopy (EIS), were conducted to evaluate the anti-corrosion efficacy of various coating formulations applied to mild steel substrates. The EP-GO/ABT-VN/MoN nanocomposite exhibited superior corrosion resistance, higher charge transfer resistance, and improved mechanical stability compared to conventional epoxy coatings and other nanocomposite formulations. The development of this high-performance coating represents a significant advancement in protective

coatings, addressing the persistent challenge of long-term durability in aggressive environments.

This study aims to synthesize and evaluate the EP/GO/ABT-VN/MoN nanocomposite for its potential as a next-generation protective coating. The key objectives include: (1) Investigating the synergistic effects of GO, ABT, and VN/MoN in enhancing corrosion resistance and mechanical performance; (2) Examining the structural, morphological, and electrochemical properties of the coatings using SEM/EDX, TEM, TGA, XRD, XPS, SECM, and EIS; (3) Assessing the long-term durability and protective performance of the nanocomposite coatings under prolonged exposure to a 3.5% NaCl solution; (4) Demonstrating the feasibility of functionalized mixed transition metal nitrides in polymer-based corrosion-resistant coatings. By addressing the current limitations of epoxy coatings, this work provides a scientific foundation for developing high-performance, durable coatings for industrial applications, including marine, aerospace, and infrastructure sectors.

1 Experimental

1.1 Materials

Graphite fine powder (325 mesh, 99.8%) was purchased from Sigma-Aldrich and used as the starting material for GO synthesis. Reagents, including sulfuric acid (H_2SO_4, 95% - 98%), phosphoric acid (H_3PO_4, 99.9%), hydrogen peroxide (H_2O_2), hydrochloric acid (HCl), and potassium permanganate ($KMnO_4$), were obtained from Merck. Hydrazine hydrate (Merck) was employed for the reduction of GO. Vanadium nitride (VN), molybdenum nitride (MoN), 2-aminobenzothiazole (ABT, ≥98%), bisphenol A diglycidyl ether epoxy resin, and an aliphatic amine hardener were also sourced from Merck. All chemicals were used as received without further purification. For coating applications, ASTM A36 mild steel strips measuring 5 cm×3 cm×0.1 cm were used, with a composition of 0.26% carbon, 0.5% manganese, 0.2% copper, 0.004% phosphorus, 0.004% sulfur, and the remainder iron. The steel samples were mechanically polished using silicon carbide sheets ranging from 250 to 1200 grit, then degreased with distilled water and acetone. After air drying at room temperature, the surface coatings were applied.

1.2 Synthesis of GO

GO was synthesized using an improved Hummer's method[41]. Initially, a homogeneous mixture was prepared by combining 360 mL of H_2SO_4 with 40 mL of H_3PO_4. Once the solution cooled to room temperature, 3 g of graphite powder was added and the mixture was stirred using a magnetic stirrer at 80 ℃ for 6 h. Following this, the solution was thoroughly washed with purified water to remove residual acids. The resulting semi-oxidized graphite was then transferred into 250 mL of H_2SO_4 to complete the oxidation process. The solution was slowly infused with 18 g of $KMnO_4$ and agitated for 4 h at 35 ℃. The resulting mixture was then diluted with 2 L of distilled water before being mixed with 40 mL of 30% H_2O_2 aqueous solution. To remove metal impurities, the mixture was filtered four times using a 0.1 M HCl solution, followed by thorough washing with distilled water until a neutral pH of 7 was achieved. Finally, the product was dried in an oven.

1.3 Synthesis of EP-GO/ABT-VN/MoN Nanocomposite

The synthesis of EP-GO/ABT-VN/MoN nanocomposites involves several key steps. Initially, 1 g of GO and 2 mL of ABT were dispersed in 150 mL of ethanol. This mixture was sonicated for 30 min to achieve uniform dispersion and then stirred at 50 ℃ for 24 h to allow the GO to be modified by ABT. After centrifugation and ethanol washing, the ABT-modified GO was dried at 80 ℃ for 24 h. To achieve homogeneous dispersion, equal volumes (1 g) of VN and MoN nanoparticles were mixed in 100 mL of distilled water, sonicated for 30 min, and then agitated for 45 min. The resulting nanoparticles were repeatedly rinsed with ethanol and distilled water to remove residual impurities, then dried at 60 ℃ for 24 h. The ABT-modified GO is subsequently combined with VN and MoN nanoparticles to form the GO/ABT-VN/MoN nanocomposites, which are then cleaned and dried for further use in coating formulations.

The GO/ABT-VN/MoN nanocomposites with various compositions (0.15%, 0.30%, 0.45%, and 0.60%) are incorporated into epoxy resin (EP) along with an aliphatic amine hardener at a 3∶1 ratio. This mixture was stirred at 3000 r/min for 2 h to ensure the formation of stable coating formulations. The resulting formulations are then applied to mild steel samples via

a spin coater, including various materials such as pure EP, EP/VN-MoN, EP-ABT/VN-MoN, EP/ABT-GO, and EP-GO/ABT-VN/MoN nanocomposites. After the coating process, the samples were air-dried at room temperature for 7 d, achieving a uniform coating thickness of 45 ± 5 μm across all tested systems. The performance of the coated samples was then evaluated before and after immersion in a 3.5% NaCl solution for 1, 15, 30, and 45 d to assess their corrosion resistance and long-term durability for various applications. The synthesis of the epoxy-GO/ABT-VN/MoN nanocomposite is represented by Eq.(1).

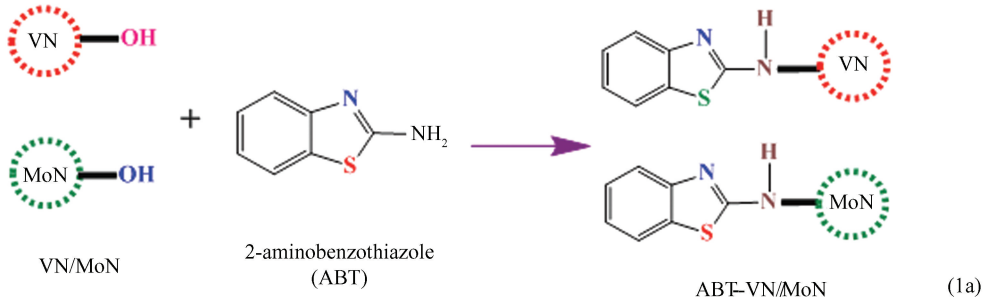

(1a)

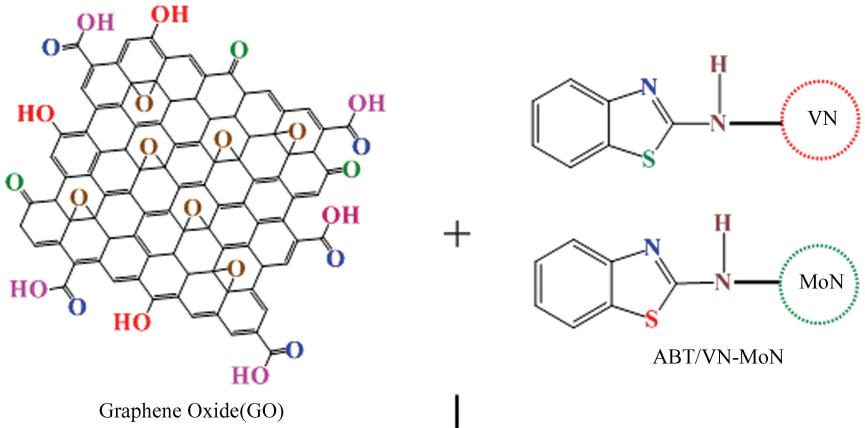

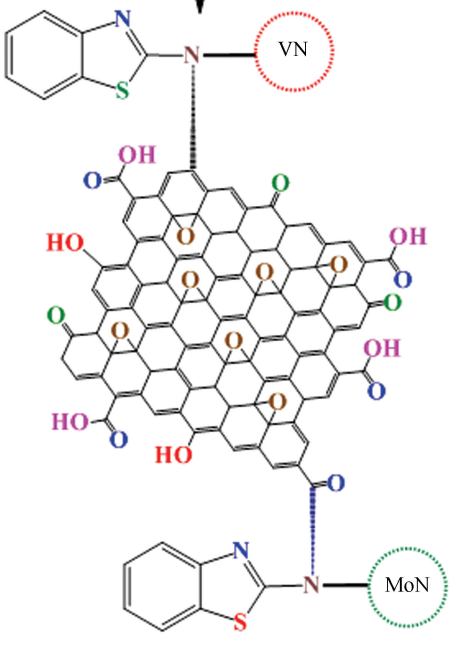

(1b)

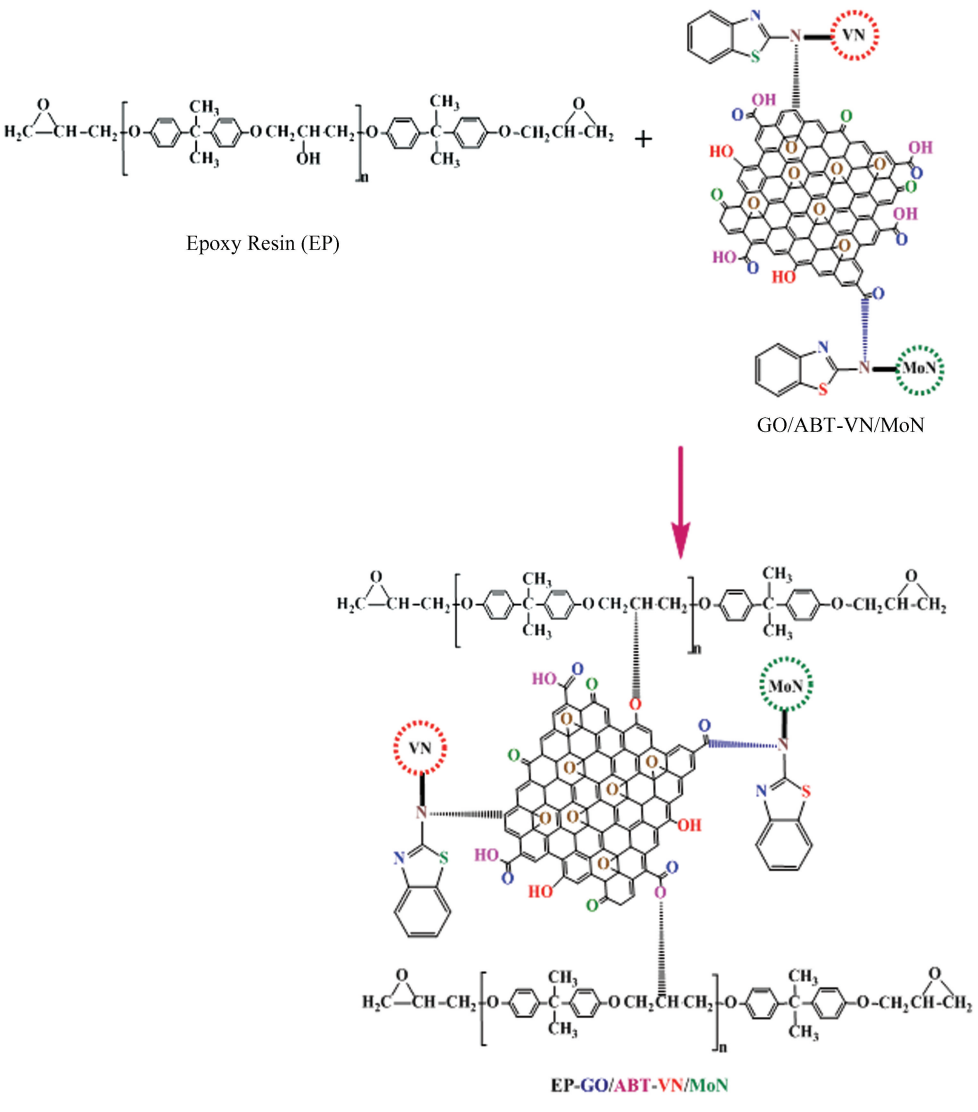

(1c)

1.4 Surface Morphology of GO/ABT-VN/MoN Nanocomposite

The microstructures and morphologies of the pristine VN/MoN, ABT/VN-MoN, GO/VN-MoN, and GO/ABT-VN/MoN nanocomposites were investigated by scanning electron microscopy (SEM, FEI-Quanta FEG 200F) coupled with energy dispersive X-ray spectroscopy (EDX). All the images were obtained at a working voltage of 25 kV. Additionally, the microstructures of the studied nanocomposites were further analyzed via transmission electron microscopy (TEM). X-ray diffraction (XRD, Bruker D8, Germany) was employed to identify the crystallographic phases present in the synthesized nanocomposites. The molecular composition and electronic states of the GO/ABT-VN/MoN nanocomposites were analyzed using X-ray photoelectron spectroscopy (XPS, PHI 5000 VersaProbe III). Thermogravimetric analysis (TGA, NETZSCH STA 449 F3 JUPITER) was conducted to evaluate the thermal stability of VN/MoN, ABT/VN-MoN, GO/VN-MoN, and GO/ABT-VN/MoN nanocomposites. The analysis was performed under an inert nitrogen atmosphere from 40 to 800 ℃ at a heating rate of 10 ℃/min.

1.5 Electrochemical Studies

EIS was employed to evaluate the electrochemical properties of pure epoxy resin (EP) and steel substrates coated with varying weight percentages (0.15%, 0.30%, 0.45%, and 0.60%) of GO@ABT-VN/MoN nanocomposite. The measurements were conducted using an Autolab PGSTAT 30 potentiostat/galvanostat (Echo Chemie B. V., Netherlands) after immersing the samples in a 3.5% NaCl solution for 1 h at 25±1 ℃. In addition, the corrosion resistance of the pure EP resin and polymer

nanocomposite coatings, specifically EP-VN/MoN, EP-ABT/VN-MoN, and EP-GO @ ABT/VN-MoN, was assessed over extended immersion periods of 1, 15, 30, and 45 d in the same NaCl solution using EIS. The experiments utilized a conventional three-electrode setup, with Ag/AgCl as the reference electrode, a platinum rod as the counter electrode, and the coated steel sample serving as the working electrode. All tests were conducted in a flat corrosion cell with a 250 mL capacity, where precisely 1 cm^2 of the coated surface was exposed to the electrolyte. EIS measurements were recorded over a frequency range of 100 kHz to 1 mHz, with a 10 mV AC perturbation centered around the open-circuit potential. The resulting data were analyzed using Nova 1.11.2 software.

The optimal weight percentage of GO/ABT-VN/MoN for steel coatings submerged in 3.5% NaCl solution for 1 d was determined using SECM (CHI920D, Austin, USA). Furthermore, SECM studies were conducted for epoxy and polymer nanocomposite EP-VN/MoN, EP-ABT/VN-MoN, and EP-GO/ABT-VN/MoN nanocomposite coated steel for 1 d and 45 d submerged in chloride solution for the detection of Fe^{2+} ions, using a tip potential of +0.60 V versus an Ag/AgCl/KCl reference electrode. The SECM system was configured with an Ag/AgCl reference electrode, a platinum wire as the counter electrode, and the coated metal sample as the working electrode. The SECM system used an optically encoded inchworm piezo motor to precisely move a 10 μm diameter Pt microelectrode along the *x*-, *y*-, and *z*-axes. Maintaining a consistent scanning height with the Pt tip ensured uniformity across the experiments. A customized bipotentiostat provided separate control over the sample and tip potentials. The Pt microelectrode was carefully set above the steel-coated sample, and a video microscope was used to guarantee accurate placement. Performing line scans and SECM mapping along the *x*-direction at a constant scan rate of 20 μm/s over the scratched area of the coated surface allowed for a detailed assessment of the corrosion behavior of the coated steel.

1.6 Mechanical Properties

The Adhesion properties, toughness, and tensile properties were performed on a variety of coatings, including pure EP, EP-VN/MoN, EP-ABT/VN-MoN, EP-GO/VN-MoN, and EP-GO/ABT-VN/MoN, before and after exposure to the electrolyte for various durations. The coating adhesive strength was measured using an Elcometer 106 instrument in compliance with ASTM D4541 specifications. Pull-off testing of the coated mild steel alloy sample was performed at a velocity of 10 mm/min until the coating detachment. Additionally, hardness measurements, following the ASTM E384 Vicker hardness standard, and tensile strength evaluations, according to ASTM D638, were performed on coated mild steel alloy samples. These comprehensive analyses offer valuable insights into the performance and durability of the coatings under exposure to the electrolyte, supporting the evaluation of their suitability for marine applications and their resistance to harsh environmental conditions.

1.7 Salt Spray Test

Under the ASTM B-117 method, mild steel coated with a nanocomposite was exposed to 3.5% NaCl solution for 45 d to evaluate its corrosion protection function. Cross-scribes ere made down to the metal surface to investigate the protective action of the coating. To check for corrosion in the designated area as well as for signs of blistering, staining, and adhesion failure, the coatings were cross-scratched in compliance with ASTM D1653, and then they were put in a salt spray chamber (QC711 Come Tech)[42-43].

1.8 Water Contact Angle Measurements

To better understand their interactions with water, the contact angles of the prepared samples, such as pure EP, EP-ABT/VN-MoN, and EP-GO/ABT-VN/MoN nanocomposites, were assessed via the sessile drop method. The contact angle was measured using a contact angle analyzer from KSV instruments in Finland with tiny droplets of distilled water. The measurements were conducted at three different locations on each coated sample, and the findings were averaged across many measurements to ensure accuracy. The impact and rebound of the water droplets were also recorded with a CAM101 video camera. This simple technique revealed information on the hydrophobicity of the materials, allowing us to uncover changes in their surface qualities and how water interacts with them.

1.9 Investigations of Corrosion Byproducts on Mild Steel

After 45 d of immersion in 3.5% NaCl solution, the materials that degrade on various polymer nanocomposites coated steel alloy surfaces, such as

pure EP, EP-VN/MoN, EP-ABT/VN-MoN, and EP-GO/ABT-VN/MoN nanocomposites, are characterized to provide useful information about their corrosion resistance. SEM/EDX techniques provide precise analysis of the microstructure of the outer layer and the chemical composition of corrosion products on coated steel alloys. This method offers comprehensive insights into corrosion mechanisms and evaluates the effectiveness of various nanocomposite coatings in corrosion protection. The XRD patterns obtained for the degradation outcomes after 45 d in the electrolyte enable the identification of distinct crystalline phases, which assist in validating the consequences of corrosion and determining their chemical structure. Furthermore, X-ray diffractometry provides further information by analyzing the structural properties of the generated degradation products.

2 Results and Discussion

2.1 Characterization of EP-GO/ABT-VN/MoN Nanocomposites

The morphology and elemental chemical content of pure VN/MoN, produced ABT-VN/MoN, GO/VN-MoN, and GO/ABT-VN/MoN nanocomposites were analyzed using SEM/EDX as illustrated in Fig.1. Fig.1(a) illustrates that the pure VN/MoN nanoparticles exhibit smooth, spherical, and agglomerated structural topologies due to their hydrophilic characteristics. The aggregation of nanocomposites can result in uneven dispersion, hence diminishing mechanical strength and increasing susceptibility to cracking[44]. Conversely, Fig.1(b) illustrates that the amalgamation of V, Mo, and N elemental compositions led to the synthesis of a pure VN/MoN nanocomposite. The functionalization of VN/MoN nanoparticles with ABT chemical groups yields a homogeneous distribution of the particles, as illustrated in Fig.1(c). The homogeneous distribution of particles results from the establishment of robust covalent connections (by –N- and –NH- linkages) between ABT and MoN/VN, respectively. This enhanced dispersion increases the efficiency and performance of the epoxy coating[45]. The peaks in Fig.1(d) represent C, S, N, V, and Mo, indicating the homogeneous distribution of VN/MoN nanoparticles within the ABT-VN/MoN nanocomposite. Fig.1(e) illustrates that the GO/ABT-VN/MoN nanocomposites are uniformly distributed without agglomeration, indicating that GO is chemically bonded to the ABT-modified VN/MoN nanoparticles. This signifies the establishment of a homogeneous distribution of VN/MoN nanoparticles across the GO and ABT, leading to the absence of pores or fissures. Consequently, the coating efficiency was enhanced. The incorporation of carbon, sulphur, nitrogen, oxygen, vanadium, and molybdenum in the GO/ABT-VN/MoN, illustrated in Fig.1(f), indicates its superior efficiency compared to the pristine VN/MoN, ABT-VN/MoN, and GO/VN/MoN nanocomposites.

The surface properties and internal composition of the produced nanocomposites, including pure VN/MoN, ABT-VN/MoN, GO/VN-MoN, and GO/ABT-VN/MoN, were analyzed via transmission electron microscopy (TEM), as depicted in Fig.2. Fig.2(a) illustrates that the VN/MoN nanoparticles are spherical, suggesting a certain level of agglomeration. The clustering of nanoparticles frequently results from their significant surface energy, hydrophilic surfaces, and van der Waals forces, which cause them to aggregate[46].

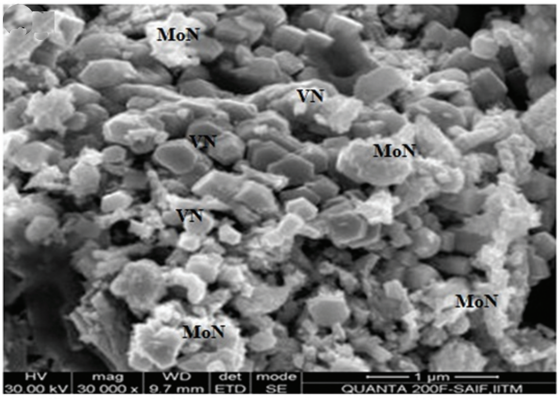

(a) SEM:VN/MoN nanoparticles

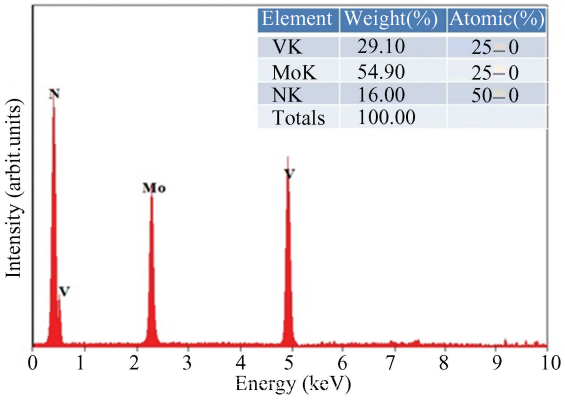

(b) EDX:VN/MoN nanoparticles

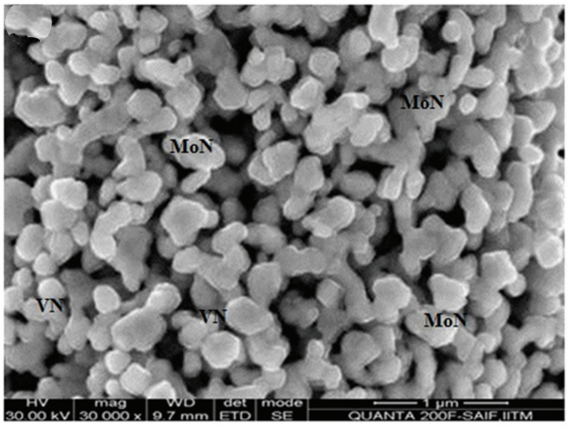

(c)SEM:ABT/VN-MoN nanoparticles

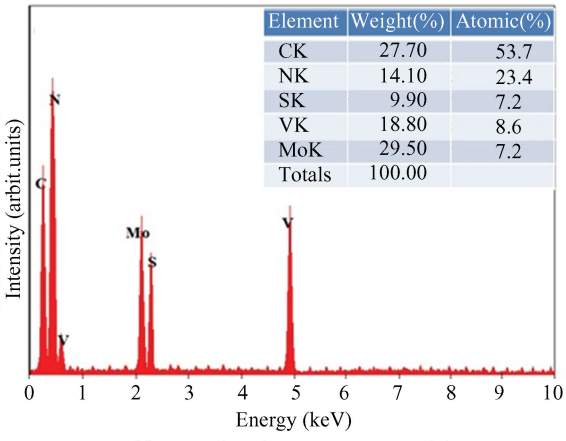

(d) EDX: ABT/VN-MoN nanoparticles

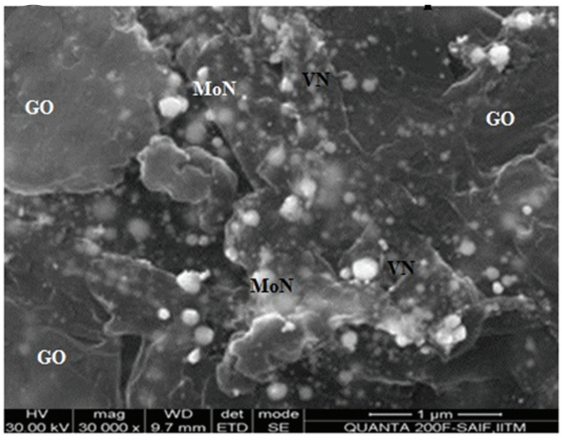

(e) SEM:GO/ABT-VN/MoN nanoparticles

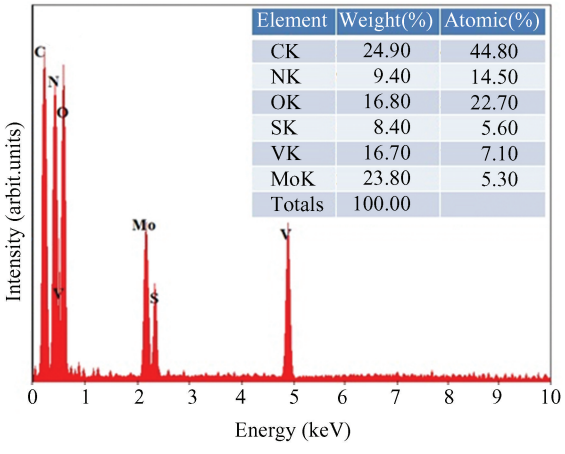

(f) EDX:GO/ABT-VN/MoN nanoparticle

Fig.1 SEM/EDX analysis of pristine VN/MoN , ABT/VN-MoN, and GO/ABT-VN/MoN nanocomposite

The functionalization of the nanoparticles with 2-aminobenzothiazole (ABT) diminished their aggregation, leading to a uniform dispersion, as illustrated in Fig.2(b). The enhancement is due to the electrostatic stability conferred by the ABT molecules, which inhibit nanoparticle aggregation. In the GO/ABT－VN/MoN nanocomposite, the VN/MoN nanoparticles are predominantly functionalized with ABT before being incorporated with GO. The chemical interaction between the ABT-modified nanoparticles and GO leads to a more even distribution, as illustrated in Fig. 2(c). This combination verifies that the nanoparticles are uniformly disseminated and densely arranged, minimizing aggregation and enhancing dispersibility. The reduction in aggregation and enhanced dispersion resulting from these functionalizations and combinations enhanced the performance of the nanocomposite.

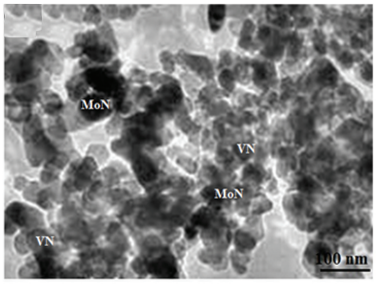

(a) Pristine VN/MoN

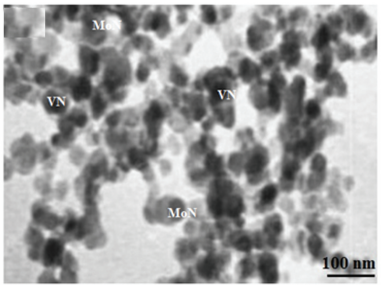

(b) ABT-VN/MoN

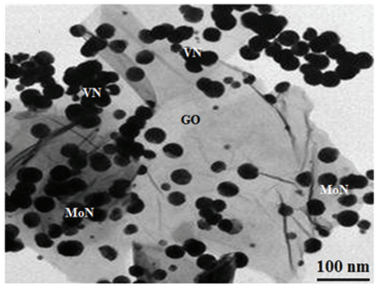

(c) GO/ABT-VN/MON

Fig.2 TEM investigation of pristine VN/MoN, ABT-VN/MoN, GO/ABT-VN/MoN nanocomposite

The elemental composition of the synthesized GO/ABT-VN/MoN nanocomposite was examined using EDX mapping, as illustrated in Fig.3, which indicated the presence of S, V, Mo, N, C, and O in the nanocomposite. The internal morphology of the GO/ABT-VN/MoN nanocomposite was examined by TEM, revealing the integration of GO into the ABT-functionalized VN/MoN nanocomposite. Due to this functionalization, a homogeneous dispersion of VN/MoN nanoparticles was found in the TEM/EDS mapping, as illustrated in Fig.3.

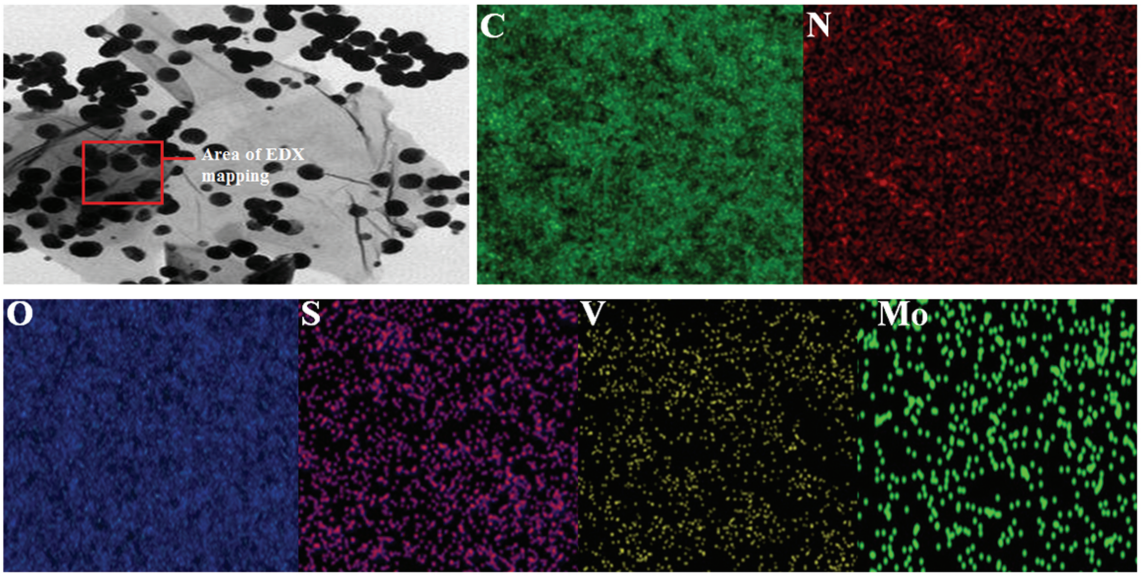

Fig.3 TEM/EDX mapping of GO/ABT-VN/MoN nanocomposite

Fig.4(a) displays the XRD pattern of the investigated compounds. Pristine VN/MoN shows distinct peaks corresponding to VN/MoN, indexed as (111), (200), (220), and (311). These reflections confirm the formation of VN and MoN phases, which have a cubic structure. ABT/VN-MoN retains the major peaks of VN/MoN, indicating that the core crystalline structure remains intact. Slight peak shifts or intensity variations may suggest ABT interactions with VN/MoN. ABT presence could lead to minor amorphous contributions, slightly altering peak broadness. In the GO/VN-MoN, the characteristic VN/MoN peaks remain, confirming their crystalline structure. The (001) peak of GO is visible at lower angles (11.1°), suggesting the presence of GO layers. No significant new peaks indicate that GO is not forming a new crystalline phase but interacting with VN/MoN. In the case of GO/ABT-VN/MoN, all major peaks from VN/MoN and GO persist. The GO (001) peak is still visible, showing retained GO structure. Possible intensity variations and peak shifts suggest synergistic interactions between GO, ABT, and VN/MoN, leading to improved dispersion and integration of components. Therefore, VN/MoN phases are confirmed in all samples. GO presence is verified by the (001) peak at low 2θ values. ABT incorporation does not disrupt VN/MoN crystallinity, but it may influence surface interactions. The GO/ABT-VN/MoN nanocomposite integrates all components while maintaining their structural integrity.

Fig.4(b) presents the TGA results for pure VN/MoN, ABT-VN/MoN, and GO/ABT-VN/MoN. The unadulterated VN/MoN sample exhibits minimal deterioration at 600 ℃. The stability of VN/MoN up to 600 °C is attributed to the development of robust covalent connections between the transition metals cobalt and chromium and nitrogen atoms. These connections create a substantial energy barrier for rupture, hence preserving the integrity of materials at elevated temperatures. The integration of VN and MoN inside a nanocomposite can produce synergistic effects and improve stability. At 250 ℃, the ABT-VN/MoN nanocomposite experiences weight reduction due to desorption of trapped volatile compounds, leading to a 7% loss in mass. Furthermore, this nanocomposite can decompose at 400 ℃, leading to the fragmentation of organic

molecules into smaller entities, which results in significant weight reduction. This decomposition entails the cleavage of C−C and C−N bonds within the ABT functional group, resulting in the liberation of volatile gases. The GO/VN/MoN nanocomposites exhibited two distinct decomposition phases. GO undergoes initial thermal degradation at temperatures exceeding 200 ℃. At 270 ℃, all residual oxygen-containing functional groups (carboxyl, hydroxyl, and epoxy) in GO can be eliminated, leading to a minimal weight loss of 3%. The second degradation transpires at roughly 520 ℃, resulting in a minimum weight loss of 13%, attributable to the considerable thermal stability of GO and the relatively stable characteristics of MoN and VN at this temperature. At 520 ℃, the GO/ABT-VN/MoN nanocomposites exhibited minimal weight loss, indicating excellent thermal stability. This stability suggests strong interactions between the VN/MoN nanocomposites and the ABT functional groups, primarily through primary and secondary amine linkages. Additionally, GO was covalently bonded to the ABT-modified VN/MoN nanoparticles via $-NH_2$ groups, contributing to the structural integrity and robustness of the composite. Consequently, the decomposition temperature increased significantly despite negligible weight loss. This resulted from the robust binding of the ABT's two secondary amino groups and two hydroxyl groups to the VN/MoN nanoparticles and GO. The study demonstrated that the GO/ABT-VN/MoN and pure VN/MoN nanocomposites exhibit exceptional stability at elevated temperatures, positioning them as viable candidates for high-temperature applications.

Fig.5 illustrates the XPS analysis of the GO/ABT-VN/MoN nanocomposite, elucidating the chemical states and interactions present within the composite. Fig.5(a) illustrates the survey spectrum of the GO/ABT−VN/MoN nanocomposite, confirming the existence of carbon, nitrogen, nickel, and manganese elements. The high-resolution C 1s spectra (Fig.5(b)) exhibit a pronounced signal at 284.4 eV, signifying C − C interactions and sp^2 hybridized carbon-carbon bonds in GO. Furthermore, the C 1s spectrum has diminished peaks at 289.9 eV and 286.5 eV, indicative of carbon-oxygen and carbon-nitrogen interactions, respectively. The signal at 285.4 eV is ascribed to carbon-hydrogen interactions, indicating that GO interacts with ABT phenyl groups. The peak at 285.9 eV signifies carbon-nitrogen interactions, particularly involving the amine groups in the ABT and MoN, VN, or GO. Fig.5(c) illustrates the N 1 s XPS spectra of ABT, featuring at 398.8 eV corresponding to −C−NH−. The deconvolution of the N 1 s spectra identifies at 400.6 eV, corresponding to $-NH_3^+$, signifying the presence of multiple nitrogen species such as secondary amines (398.6 eV) and protonated amines, which are essential for interactions among ABT, MoN, VN, and GO. Fig.5(d) illustrates that the deconvolution of the S 2p spectrum produces two distinct peaks at 161.7 eV and 162.6 eV. The peaks corresponding to $S2p_{3/2}$ and $S2p_{1/2}$ indicate the presence of −SH groups in ABT.

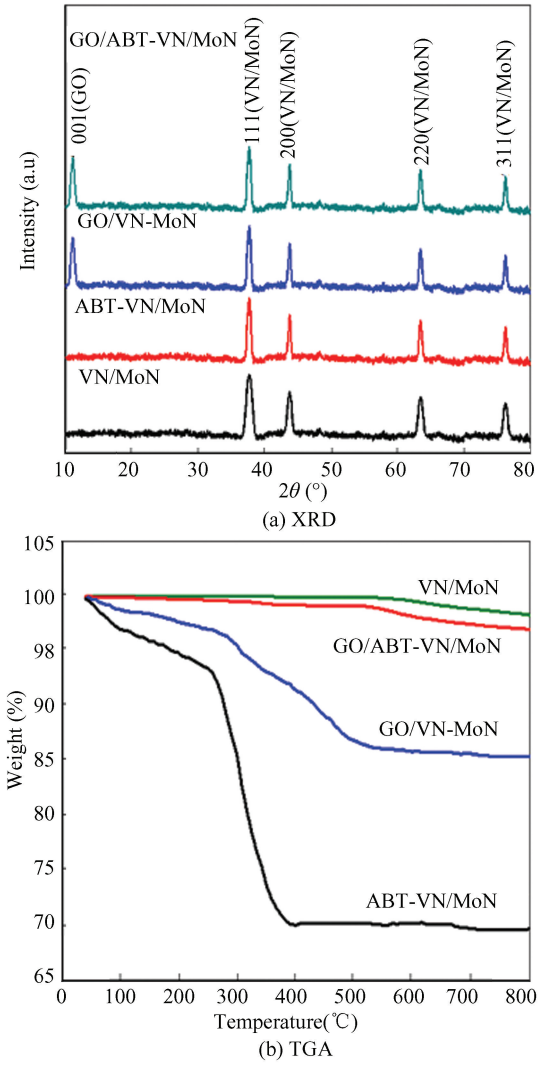

Fig.4 XRD patterns and TGA analysis of pristine VN/MoN, ABT-VN/MoN, GO/VN-MoN, and GO/ABT-VN/MoN nanocomposite

Fig.5(e) presents the V 2p spectrum, which

shows deconvoluted peaks for V $2p_{3/2}$ and V $2p_{1/2}$ with binding energies of 515.8 eV and 524.1 eV, respectively, signifying the presence of vanadium in the +3 oxidation state. Fig.5(f) illustrates the Mo 3d spectrum, featuring peaks for Mo $3d_{5/2}$ and Mo $3d_{3/2}$ with binding energy values of 232.9 eV and 235.8 eV, respectively, indicating that manganese exists in the +3 oxidation state.

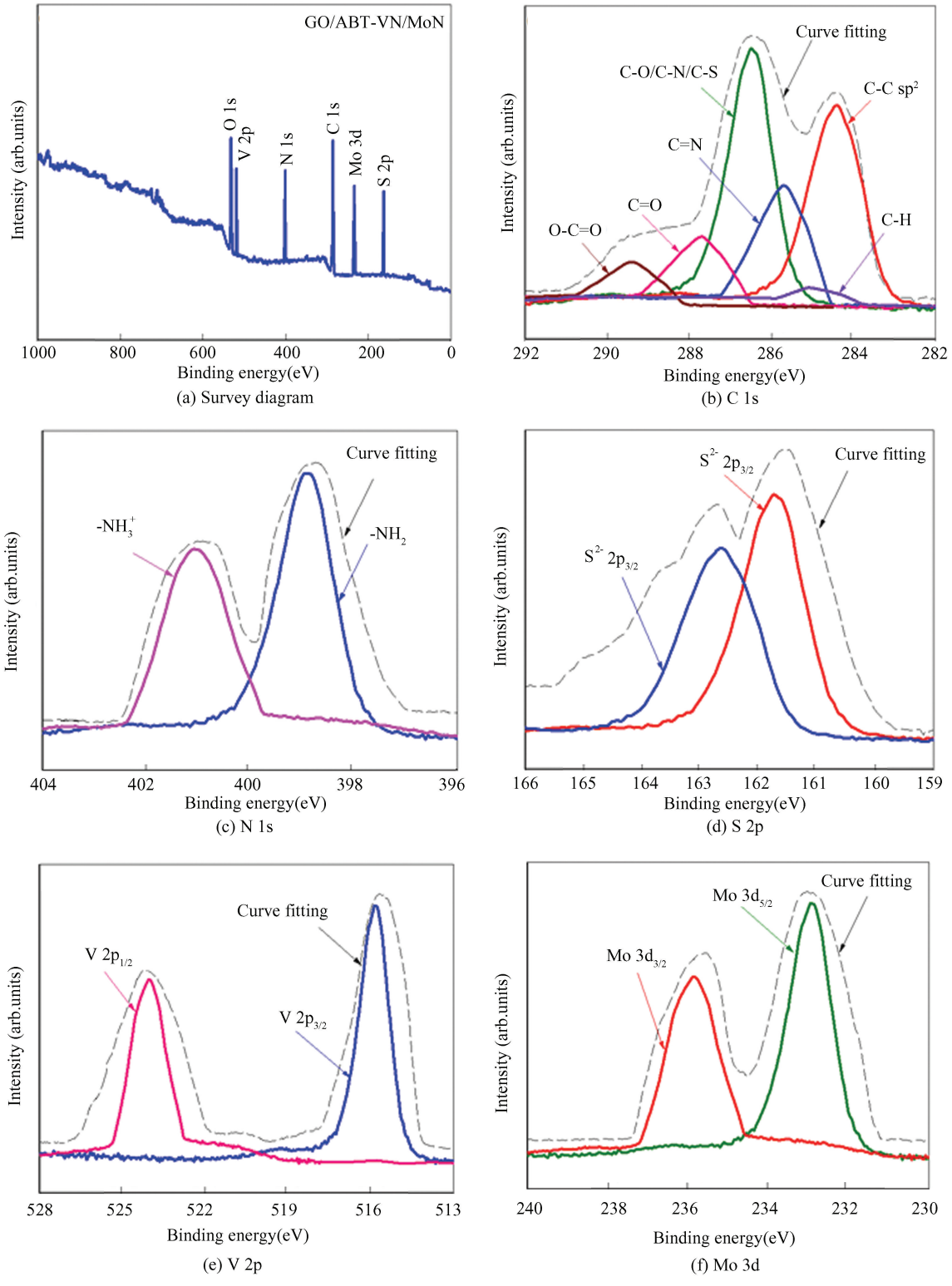

Fig.5 XPS analysis of GO/ABT-VN/MoN nanocomposite

2.2 Corrosion Resistance of EP-GO/ABT-VN/MoN Nanocomposites

2.2.1 SECM examination

SECM analysis was conducted on mild steel samples coated with several weight percentages of EP-GO/ABT-VN/MoN nanocomposites (0.15%, 0.30%, 0.45%, and 0.60%) to determine the optimal composition. The polymer nanocomposite-coated steel alloys with varying weight compositions were immersed in a 3.5% NaCl solution for one day at a tip potential of +0.60 V versus the Ag/AgCl reference electrode, which was employed to detect ferrous ions through their oxidation to ferric ions, as illustrated in Fig.6.The SECM images illustrate the degradation of the coated specimens via various color variations, emphasizing the regions of anodic and cathodic activity. The EP-GO/ABT-VN/MoN nanocomposite at an optimal weight percentage of 0.45% demonstrated a significantly reduced current of 1.0 nA, compared to 5.0 nA for 0.15%, 3.2 nA for 0.30%, and 2.1 nA for 0.60%, showing enhanced corrosion protection. The 0.15% EP-GO/ABT-VN/MoN nanocomposite created a thin, permeable layer on mild steel alloy, allowing corrosive ions to penetrate easily and promoting increased formation of corrosion byproducts on the surface.

Increasing the concentration to 0.30% improved the coating thickness, thereby reducing the infiltration of corrosive ions and providing a slight improvement in the coating's resistance to corrosion. The nanocomposite, at 0.45%, produces an efficient, impermeable coating that surpasses previous formulations in corrosion resistance. At a concentration of 0.60%, nanoparticle aggregation leads to the development of fractures and micropores, facilitating the generation of corrosion products through these micropores. Consequently, the coating's resistance to corrosion was marginally inferior to that of the 0.45% sample. The best concentration of the EP-GO/ABT-VN/MoN nanocomposite for further exploration is established at 0.45%.

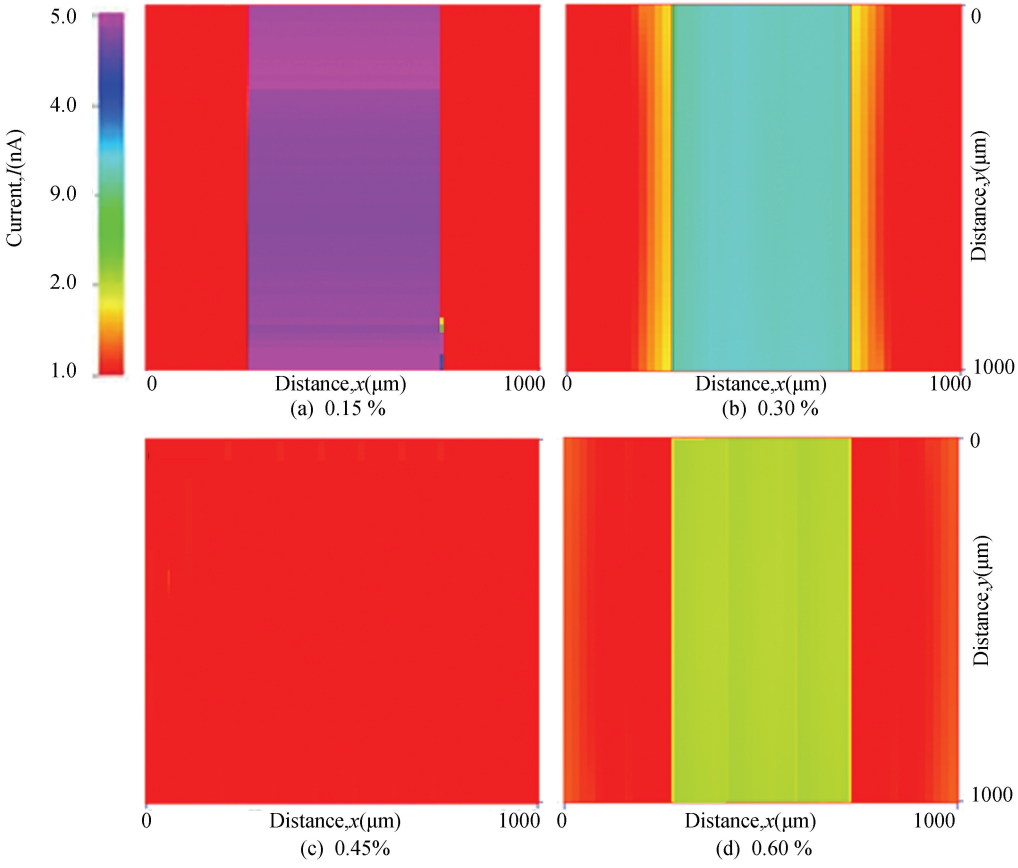

Fig.6 SECM analysis of mild steel coated with various percentages of GO/ABT-VN/MoN nanoparticles, 0.15 %, 0.30 %, 0.45 %, and 0.60 % for 1 d immersion in 3.5% NaCl solution at tip potential of +0.60 V vs. Ag/AgCl/KCl reference electrode for the detection of ferrous ions

Fig.7 displays SECM results of nanocomposite-coated steel alloys, which were immersed in a 3.5% NaCl solution for durations of 1 d and 45 d, with ferrous ions detected at +0.60 V. The substantial current increments for the pure epoxy coating rise from 8.5 nA to 24.8 nA as exposure extends from 1 d to 45 d. The corrosion process is accelerated by the weak adhesive force of the epoxy and the full exposure of the epoxy-coated steel alloy to the 3.5% NaCl solution via the micropores in the epoxy covering. The current for the EP-VN/MoN polymer nanocomposite increased from 4.5 nA to 12.8 nA as exposure to a 3.5% NaCl solution extended from 1 d to 45 d, respectively. The modest increase in current can be attributed to the incorporation of VN and MoN nanoparticles, which effectively block the micropores within the epoxy matrix, thereby enhancing the barrier properties of the coating. Prolonging the submersion period from 1 d to 45 d in a 3.5% NaCl solution caused the nanoparticles to agglomerate on the polymer covering, leading to an increase in the current value. The EP-ABT/VN-MoN nanocomposites exhibit a slight current variation from 3.1 nA to 6.2 nA across immersion durations of 1 d and 45 d in a 3.5% NaCl solution, respectively. The functionalization of VN and MoN nanoparticles with ABT through the primary and secondary amino groups facilitates effective adhesion to the steel alloy surface, leading to a homogeneous dispersion of ABT-functionalized VN/MoN nanoparticles within the epoxy matrix and enhancing coating resistance. GO was integrated into the ABT functionalized VN/MoN nanoparticles within the epoxy matrix to enhance the coatings' durability. After 1 d of immersion, the EP-GO/ABT-VN/MoN nanocomposite-coated steel exhibited a current of 1.0 nA, which increased to 1.6 nA after 45 d, indicating minimal iron degradation to Fe^{2+} ions over time. The EP-GO/ABT-VN/MoN nanocomposite demonstrates a minimal rise in current compared to other formulations, indicating superior corrosion resistance. This performance is attributed to strong covalent interactions between the hydroxyl groups of GO and the secondary amine functionalities present on ABT-modified VN/MoN nanoparticles.

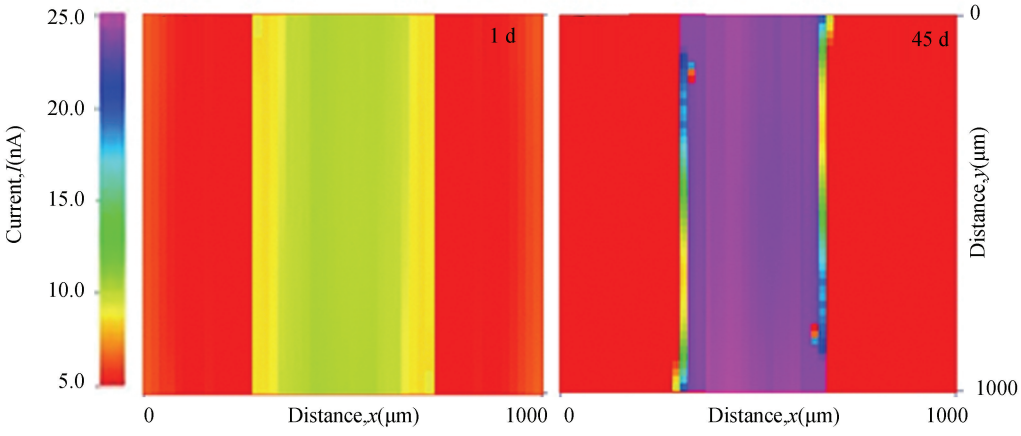

(a) Epoxy

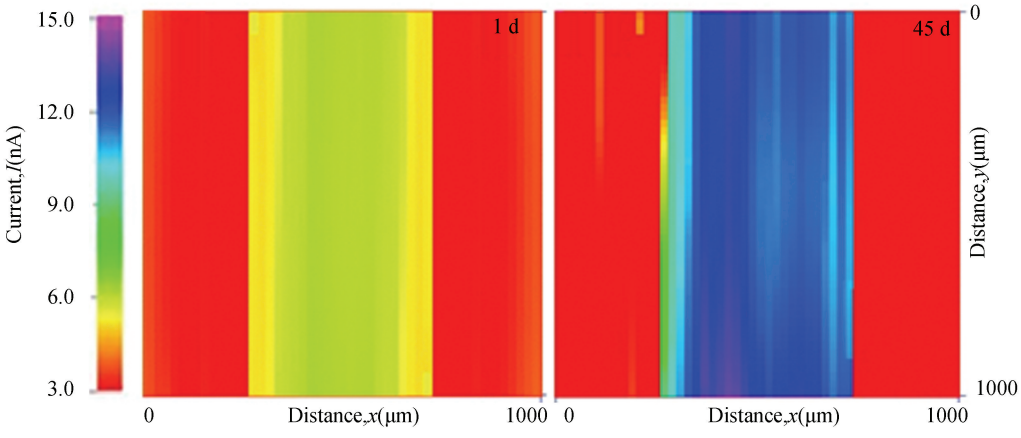

(b) EP-VN/MoN

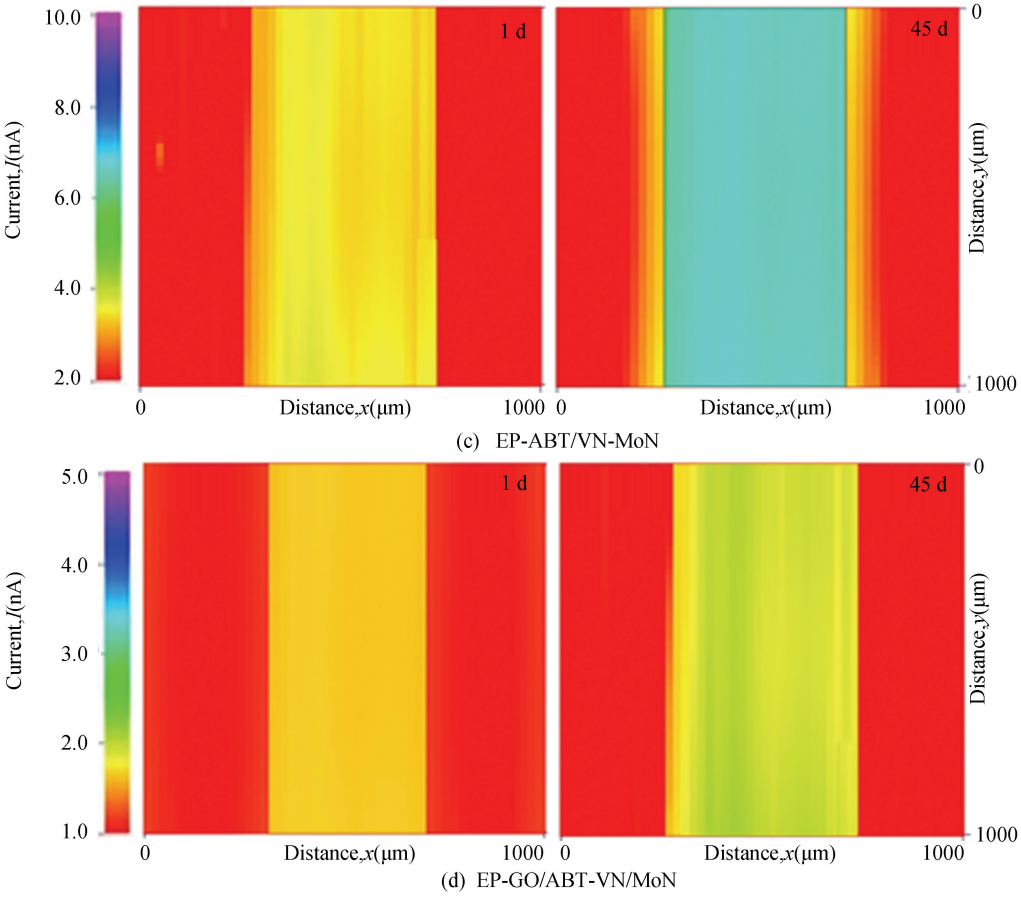

Fig. 7 SECM analysis of epoxy, EP-VN/MoN, EP-ABT/VN-MoN, and EP-GO/ABT-VN/MoN nanocomposite coated steel for 1 d and 45 d immersion in 3.5% NaCl solution for the detection of Fe^{2+} ions at tip potential +0.60 V vs. Ag/AgCl/KCl reference electrode

The lone electron pairs on nitrogen atoms play a critical role in suppressing oxidation reactions on the metal surface by donating electron density, which contributes to the formation of uniform and stable coatings. Furthermore, the strong interfacial interactions within the VN/MoN nanocomposite matrix enhance the overall bonding strength, resulting in lower current densities and improved corrosion protection for the steel alloy substrates.

2.2.2 *Analysis of EIS*

Fig.S1 illustrates the standard EIS diagram of pure EP resin and EP coatings with varying weight percentages of 0.15%, 0.30%, 0.45%, and 0.60% GO/ABT-VN/MoN nanocomposite applied to mild steel alloy exposed to the chloride media for 1 d, aimed at determining the optimal weight percentage of coating for enhanced anti-corrosion protection. The overall diameter of the semicircle in the Nyquist plot of the pure epoxy coating was markedly reduced, as illustrated in Fig.S1. This results from nonuniform dispersion and the existence of pores in the epoxy coating. Consequently, pure epoxy-coated mild steel exhibits increased susceptibility to corrosive ions through existing pores, resulting in the generation of additional degradation components. After 1 d immersion in the electrolyte, the diameter of the semicircle in the Nyquist plot increased from 0.15% to 0.45% for the epoxy encased with the GO/ABT-VN/MoN nanocomposite. In Nyquist plots, the semicircle's diameter enlarges with an increase in the percentage composition of the nanocomposites. Fig.S1 illustrates that the semicircle's width in the Nyquist plot expands when the mild steel alloy is coated with 0.45% GO/ABT-VN/MoN. The effective functionalization of the nanocomposites resulted in a uniformly distributed coating on the surface of mild steel, significantly hindering the ingress of corrosive ions from the 3.5% NaCl solution. Fig. S1 illustrates that an increase in percentage composition to 0.60% resulted in a reduction of the semicircle diameter in the Nyquist plot, in comparison to 0.45%. The resistance of the coatings diminished as the composition increased by

0.60%, attributable to the aggregation of nanoparticles on the polymer coating, leading to irregular films on the steel. The diffusion channel becomes susceptible to corrosive ions, resulting in the generation of additional degradation components. This study revealed that including 0.45% GO/ABT-VN/MoN nanocomposites into the EP matrix achieved an optimal weight percentage of the coated alloy steel, aligning with the findings from the SECM analysis.

Fig.8 demonstrates the Nyquist plots acquired for mild steel alloys covered with pure EP, EP-VN/MoN, EP-ABT/VN-MoN, and EP-GO/ABT-VN/MoN nanocomposites, all immersed in a 3.5% NaCl solution for durations of 1, 15, 30, and 45 d, respectively. Figs. S2 and S3 show the related Bode plots. Fig. 8 illustrates that all coated samples in the Nyquist plot demonstrate exceptional corrosion resistance following immersion in a 3.5% NaCl solution for one day. In comparison to other nanocomposites, the EP-GO/ABT-VN/MoN nanocomposite (optimal percentage: 0.45%) coated on mild steel alloy exhibits the highest resistance, surpassing pure EP, EP-VN/MoN, and EP-ABT/VN-MoN nanocomposite coatings on steel alloy submerged in a 3.5% NaCl solution for durations of 1, 15, 30, and 45 d. This resistance arises from the strong interaction between GO and ABT-functionalized VN/MoN nanoparticles, mediated by the secondary amino groups of ABT, which promotes uniform nanoparticle distribution within the EP coating and forms a cohesive layer on the alloy surface. Electrochemical parameters were obtained using an equivalent circuit model, as shown in Fig. S4, which was constructed by fitting the Nyquist spectra with ZsimpWin software. To describe the uncoated mild steel and the nanocomposite coatings EP, EP-VN/MoN, EP-ABT/VN-MoN, and EP-GO/ABT-VN/MoN after 1, 15, 30, and 45 d of immersion in a 3.5% NaCl solution, the EIS spectra were analyzed using the models $\{R_{ct}\ C_{dl}\}$ and $\{R_s\ (R_{coat}\ CPE_{coat})\ (R_{ct}\ CPE_{dl})\}$.

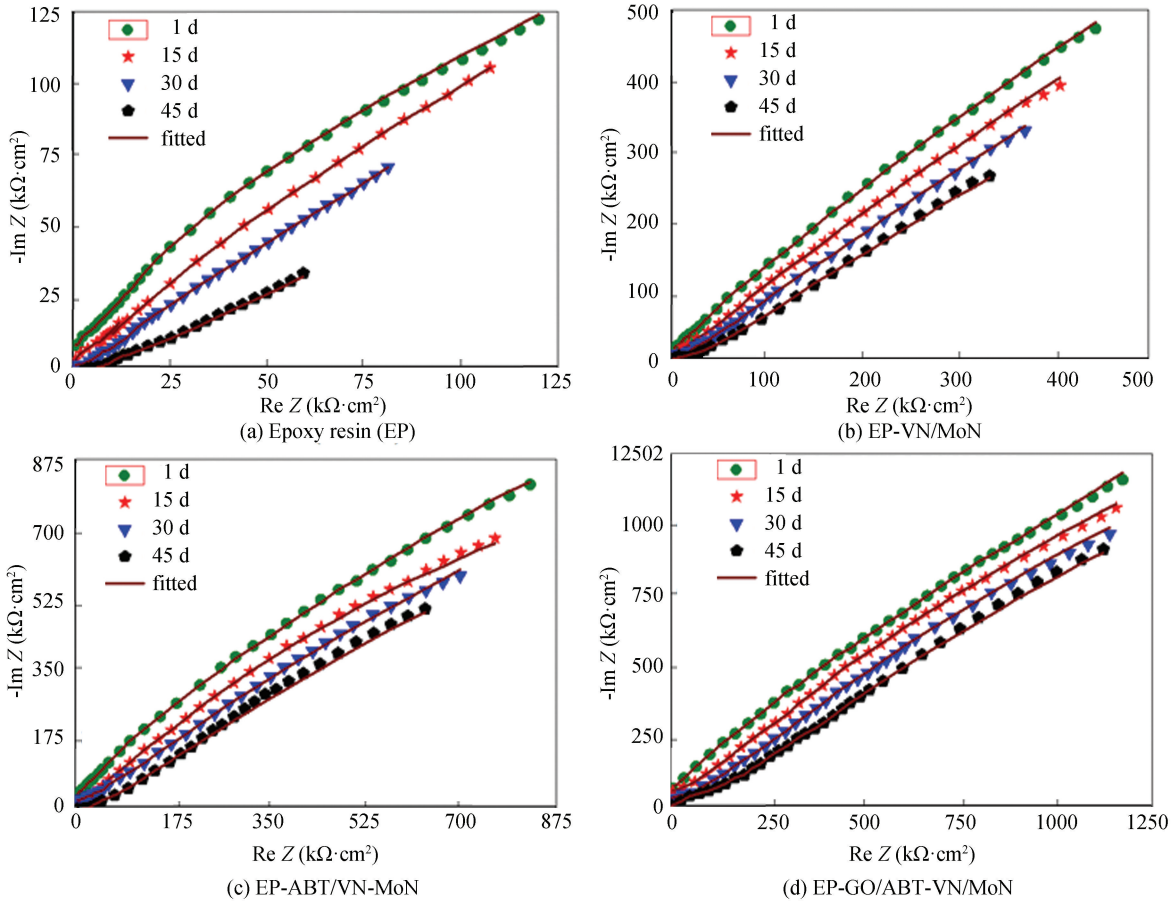

Fig. 8 Nyquist plots for EP, EP-VN/MoN, EP-ABT/VN-MoN, and EP-GO/ABT-VN/MoN nanocomposite coated steel after 1, 15, 30, and 45 d of immersion in 3.5% NaCl solution (*Z*: Impedance)

The charge transfer resistance (R_{ct}) and double layer capacitance (C_{dl}) are the circuit components of uncoated mild steel. Additionally, R_s, R_{coat}, R_{ct}, CPE_{coat}, and CPE_{dl} are circuit elements of the nanocomposite-coated mild steel alloy, denoting solution resistances of electrolyte, coating, charge transfer, the coating's constant phase element, and double layer capacitance, respectively. The quality of the equivalent circuit fitting was further evaluated using chi-square (χ^2) values, providing a quantitative measure of the reliability of the fitting results.

Table 1 presents the fitted parameters for both uncoated mild steel and coated nanocomposites.

Table 1 The fitted results of EIS using equivalent circuit

Samples	Time(d)	R_s ($\Omega \cdot cm^2$)	R_{coat} ($\Omega \cdot cm^2$)	CPE_{coat}(μF)	R_{ct} ($\Omega \cdot cm^2$)	CPE_{dl}(μF)	$\chi^2\times10^{-4}$
Bare mild steel	1	106	–	–	6.35×10^3	503.5	1.9
	15	95	–	–	2.54×10^3	732.3	1.7
	30	83	–	–	8.50×10^2	985.5	2.9
	45	65	–	–	4.10×10^2	1340.1	2.1
Epoxy resin (EP) coating	1	120	2.75×10^5	74.5	2.82×10^5	348.4	2.3
	15	106	1.36×10^5	130.3	1.86×10^5	566.9	2.2
	30	100	5.55×10^4	163.6	6.10×10^4	750.2	3.1
	45	90	1.46×10^3	180.8	3.05×10^3	924.4	2.9
EP-VN/MoN coating	1	128	9.57×10^7	48.7	1.60×10^8	295.3	1.7
	15	121	6.59×10^7	88.2	7.47×10^7	460.5	1.1
	30	113	3.85×10^7	103.3	4.65×10^7	647.3	2.2
	45	105	1.64×10^7	122.1	2.75×10^7	770.2	2.0
EP-ABT/VN-MoN coating	1	154	8.25×10^8	33.5	9.75×10^9	205.9	1.7
	15	149	7.23×10^8	58.7	7.71×10^9	342.1	3.1
	30	141	5.30×10^8	73.6	5.64×10^9	447.4	2.6
	45	134	3.44×10^8	98.5	3.40×10^9	548.7	1.7
EP-GO/VN-MoN coating	1	163	7.69×10^9	18.1	9.75×10^{10}	159.4	1.4
	15	158	6.15×10^9	26.5	8.77×10^{10}	265.6	2.0
	30	151	4.76×10^9	30.7	7.12×10^{10}	349.2	2.6
	45	146	3.17×10^9	48.2	5.25×10^{10}	465.8	1.6
EP-GO/ABT-VN/MoN coating	1	287	1.15×10^{13}	9.5	1.53×10^{13}	19.2	2.1
	15	284	9.57×10^{13}	14.7	9.95×10^{12}	38.5	1.6
	30	280	8.95×10^{13}	21.5	9.37×10^{12}	68.4	2.3
	45	276	8.50×10^{13}	30.5	8.89×10^{12}	94.1	1.7

The EP-GO/ABT-VN/MoN nanocomposite exhibited a coating resistance of 1.15×10^{13} $\Omega \cdot cm^2$ after 1 d and 1.53×10^{13} $\Omega \cdot cm^2$ during 45 d of exposure to the electrolyte. Following 1 d of immersion in a 3.5% NaCl solution, the coating resistance values for pure epoxy, EP-VN/MoN, EP-ABT/VN-MoN, and EP-GO/VN-MoN nanocomposites were recorded as 2.75×10^5 $\Omega \cdot cm^2$, 9.57×10^7 $\Omega \cdot cm^2$, 8.5×10^8 $\Omega \cdot cm^2$, and 7.69×10^9 $\Omega \cdot cm^2$, respectively. Following 45 d of immersion in a 3.5% NaCl solution, the resistance of the nanocomposite coatings decreased to 1.46×10^3 $\Omega \cdot cm^2$, 1.64×10^7 $\Omega \cdot cm^2$, 3.44×10^8 $\Omega \cdot cm^2$, and 3.17×10^9 $\Omega \cdot cm^2$. Following immersion in a 3.5% NaCl solution, the resistivity of the EP-GO/ABT-VN/MoN nanocomposite coating improved due to the robust covalent bonds formed between the hydroxyl groups of GO and the secondary amino groups of the ABT-modified VN/MoN nanoparticles. Upon functionalization of GO on ABT-modified VN/MoN nanoparticles, a homogeneous distribution of VN/MoN nanoparticles on the epoxy coating was achieved, in contrast to earlier nanocomposites. The synergistic effect of nanocomposites enhances adhesion strength, hence augmenting the anti-corrosive capabilities of the coatings following 45 d of immersion in a 3.5% NaCl solution. The EP-GO/ABT-VN/MoN nanocomposite-coated steel alloy exhibited stable corrosion resistance during prolonged electrolyte immersion, indicating superior adhesion strength on the steel surface.

In comparison to other nanocomposite coatings, the R_{ct} of pure epoxy coating diminished from $2.82\times$

$10^5\ \Omega \cdot cm^2$ to $3.05\times10^3\ \Omega \cdot cm^2$ following 45 d of exposure to the electrolyte. This score indicates the coating's inadequate corrosion resistance due to micropores and cracks, which facilitate the infiltration of negative ions and initiate the corrosion process. Following 45 d of exposure to the electrolyte, the EP-VN/MoN nanocomposites exhibited a moderate reduction in R_{ct}, decreasing from $1.60\times10^8\ \Omega \cdot cm^2$ to $2.75\times10^7\ \Omega \cdot cm^2$. Nonetheless, its value remains superior to that of pure epoxy covering. This results from the incorporation of nanoparticles into the epoxy coating. Nevertheless, the poor adhesive force of the epoxy led to the agglomeration of nanoparticles on the coating, resulting in uneven surfaces. Consequently, Cl^- ions rapidly infiltrate the mild steel surface, resulting in quick corrosion. Following 45 d of exposure to the electrolyte, the R_{ct} of the EP-ABT/VN-MoN nanocomposite coating decreased from $9.75\times10^9\ \Omega \cdot cm^2$ to $3.40\times10^9\ \Omega \cdot cm^2$. The functionalization of VN/MoN with ABT transpires via the reactivity of the amino groups present in ABT. Consequently, the EP-ABT/VN-MoN nanocomposite coating demonstrates superior efficacy compared to the EP/VN-MoN and pure EP nanocomposites. The charge transfer resistance of the coatings decreased from $9.75\times10^{10}\ \Omega \cdot cm^2$ to $5.25\times10^{10}\ \Omega \cdot cm^2$ for EP-GO/VN/MoN nanocomposites during 45 d of exposure to the electrolyte, occurring due to the contacts between GO and VN/MoN nanoparticles facilitated by covalent bonding, electrostatic attraction, $\pi-\pi$ interactions, and other mechanisms. These interactions improve the stability and distribution of the nanoparticles on the GO surface. The bonding strength of the nanocomposite to mild steel is diminished, as it is less effective than the EP-GO/ABT-VN/MoN nanocomposite. Consequently, following 45 d of exposure to the electrolyte, the EP-GO/ABT-VN/MoN nanocomposite coated mild steel alloys demonstrate significant charge R_{ct}, coating resistance (R_{coat}), solution resistance (R_s), and C_{dl}. The results demonstrated that organic molecules containing multiple functional groups and highly electronegative atoms show enhanced coordination with VN/MoN nanoparticles. This results in a uniform dispersion within the epoxy coating, potentially functioning as an efficient nanocomposite barrier layer over the mild steel surface.

Figs.S2 and S3 present Bode resistance and Bode phase graphs for pure EP, EP-VN/MoN, EP-ABT/VN-MoN, and EP-GO/ABT-VN/MoN nanocomposites exposed to the electrolyte for durations of 1, 15, 30, and 45 d. Fig. S2 illustrates the Bode plot of the logarithm of the impedance magnitude ($\log|z|$) against the logarithm of the frequency ($\log f$) for pure EP, EP-VN/MoN, EP-ABT/VN-MoN, and EP-GO/ABT-VN/MoN nanocomposite – coated mild steel alloys immersed in a 3.5% NaCl solution for durations of 1, 15, 30, and 45 d, respectively. The impedance diminishes with rising frequency for all coatings, demonstrating the capacitive characteristics of the nanocomposites, as illustrated in Fig.S2. Moreover, as the period of immersion grew, the impedance diminished, signifying a reduction in the protective efficacy of the coatings[47]. The impedance of the pure epoxy glue decreased with a prolonged immersion period. The existing pores in the epoxy resin deteriorate over time, allowing more corrosive elements to infiltrate and so reducing its resistance.

In comparison to the pure epoxy coating, the EP-VN/MoN nanocomposite coating exhibits superior impedance consistently. The incorporation of VN and MoN nanoparticles enhanced the barrier characteristics, increasing corrosion resistance. The EP-ABT/VN-MoN nanocomposite coating exhibited significantly greater impedance compared to the EP-VN/MoN nanocomposite and pure epoxy resin. The increased impedance verifies that the ABT employed to functionalize the VN and MoN nanoparticles further improves corrosion resistance. The EP-GO/ABT-VN/MoN composite has the highest impedance values across various frequencies and immersion durations, signifying superior corrosion resistance. The elevated impedance at low frequencies indicates effective barrier properties, demonstrating that GO enhances mechanical stability and dispersion. The coatings' resistance to 3.5% NaCl solution was enhanced by the synergistic effects of ABT and VN-MoN. Fig. S3 illustrates the Bode phase plot, showcasing the phase angle (θ) against the logarithm of frequency ($\log f$) for a 3.5% NaCl solution. With an increase in immersion duration, the phase angle diminishes, indicating a reduction in capacitive properties and consequently a drop in the protective efficacy of the films. When the exposure duration increased, the phase angle of pure epoxy resin somewhat decreased, indicating a partial loss of capacitive properties. The capacity of epoxy resin to function as a barrier progressively diminishes, facilitating increased ionic

conduction as it deteriorates. The phase angle of EP-VN/MoN exceeds that of pure epoxy and maintains comparable stability. The integration of VN/MoN nanoparticles enhances capacitive behavior compared to pure epoxy, signifying superior barrier performance. The ABT component in the EP-ABT/VN-MoN nanocomposite further augments the capacitive behavior, enhancing the overall barrier characteristics and resulting in the establishment of more stable phase angles. Conversely, the EP-GO/ABT-VN/MoN composite maintains more pronounced phase angles during immersion, leading to extended capacitive behavior and enhanced corrosion resistance. This attribute is significant as it indicates the coatings' capacity to maintain charge and function as an effective barrier against corrosive agents. The use of GO, ABT, and VN-MoN in the nanocomposite coating enhanced mechanical stability and augmented the corrosion resistance of the coatings. Table 2 presents the coating and charge transfer resistances of the previously characterized nanocomposites[48-60].

Table 2 Comparison of electrochemical study of different polymer nanocomposites

S.No	Nanocomposites	Electrolyte medium	Coating resistance R_{coat} ($\Omega \cdot cm^2$)	Charge transfer resistance (R_{ct}) ($\Omega \cdot cm^2$)	Reference
1	EP-GCN/EAMS-TiO_2	Natural seawater	9.05000×10^{10}	9.53000×10^{12}	[48]
2	PU/SiO_2-Al_2O_3	3.5 % NaCl solution	7.56030×10^{5}	1.43987×10^{6}	[49]
3	EP-APTES-MoO_3	Natural seawater	-	5.90000×10^{4}	[50]
4	PU/ABTA/AlN	Seawater	5.01200×10^{5}	5.20200×10^{6}	[51]
5	GO/h-BN/WBE	5wt% NaCl	1.44000×10^{4}	4.35000×10^{4}	[52]
6	gC_3N_4@ SiO_2(0.5wt %)	3.5wt% NaCl	4.20900×10^{6}	2.75300×10^{6}	[53]
7	FGO+EP	3.5 % NaCl	1.23900×10^{4}	1.11400×10^{5}	[54]
8	EP-imidazole-GO	3.5 % NaCl	-	1.56344×10^{5}	[55]
9	EP-PANI-GO	3.5 % NaCl	2.70000×10^{6}	8.00000×10^{5}	[56]
10	EP/CaFe-TTA LDH@ g-C_3N_4	3.5 % NaCl	8.75000×10^{7}	2.16000×10^{8}	[57]
11	TiO_2-GO-f-EP	3.5 % NaCl	1.49000×10^{5}	2.28000×10^{7}	[58]
12	EP/GCN/APTES-Nb_2O_5	Seawater	5.97000×10^{9}	5.70000×10^{11}	[59]
13	EP/GCN/MEPS/Ta_2O_5	Seawater	6.67000×10^{10}	6.20000×10^{12}	[60]
14	EP-GO/ABT-VN/MoN	3.5 % NaCl	1.15000×10^{13}	1.53000×10^{13}	Present work

2.2.3 Salt spray test

Salt spray analysis was conducted to examine the anti-corrosion capabilities of pure epoxy EP-VN/MoN, EP-ABT/VN-MoN, and EP-GO/ABT-VN/MoN, coated on mild steel after 45 d of exposure to the electrolyte. Figs. S5(a)-(d) illustrate the visual representations of the scratched covered samples. The presence of micropores in the coating reduced the effectiveness of corrosion protection provided by the pure epoxy layer on mild steel. Corrosive ions can readily infiltrate the micropores of the epoxy coating, leading to the formation of brown rust (a mixture of iron hydroxides) on the surface, as illustrated in Fig. S5(a). The incorporation of VN/MoN nanoparticles into the epoxy coating enhanced its corrosion resistance slightly by successfully occluding micropores. Nonetheless, uniform dispersion was not achieved because of the aggregation of VN/MoN on the coating, leading to the development of corrosion components in the cross-scratched region, as illustrated in Fig.S5(b). Fig.S5(c) illustrates that the production of rust surrounding the scratched region is significantly reduced in relation to the functionalization of the VN/MoN nanoparticles by the amino groups of the ABT in EP-ABT/VN-MoN. In the EP-GO/ABT-VN/MoN nanocomposite coated mild steel, the functionalization of VN/MoN is facilitated by both ABT and GO, leading to the creation of an efficient barrier and a homogeneous dispersion coating, as illustrated in Fig. S5(d). Consequently, corrosive ions encounter challenges in infiltrating the coating, thereby impeding the formation of corrosion products in the vicinity of the scratched area. This investigation demonstrates that the EP-GO/ABT-VN/MoN nanocomposite-coated mild steel alloy serves as a protective barrier against corrosion.

2.3 X-ray Diffraction Studies

Following 45 d of exposure to the electrolyte, Fig.9 illustrates the XRD analysis of coated mild steel alloys. The unique peaks align with the crystal structures of GO, VN, and MoN, together with corrosion products such as γ-FeOOH (lepidocrocite) and Fe_2O_3 (hematite) formed on the surface of the steel exposed to the electrolyte. The corrosion peaks of γ-FeOOH and Fe_2O_3 correspond to 2θ values of 29.3°, 34.2°, 46.7°, 587.8°, and 38.2°, respectively. When mild steel is immersed in a 3.5% NaCl solution, an electrochemical reaction transpires, wherein Fe reacts with O_2 and H_2O to produce $Fe(OH)_2$ during the initial oxidation phase. Upon the subsequent oxidation of $Fe(OH)_2$, the products include $Fe(OH)_3$, Fe_2O_3 (hematite), Fe_3O_4 (magnetite), and other oxyhydroxides such as α-FeOOH (goethite) and γ-FeOOH (lepidocrocite). The epoxy-coated mild steel exhibits peak intensity for γ-FeOOH (lepidocrocite) and a trough intensity for Fe_2O_3. The coating exhibits significant porosity and lacks uniformity. Micropores within the coating compromised the corrosion resistance performance of mild steel coated with pure epoxy. The VN/MoN nanoparticles were integrated into the epoxy coating, exhibiting maximum intensity peaks for the MoN/VN nanoparticles at 42.6°. The corrosion products of γ-FeOOH and Fe_2O_3 exhibited a minor decrease in peak intensity. This indicates that the protective efficacy of the epoxy coating and its pores was obstructed by the MoN and VN nanoparticles, hence impeding the ingress of corrosive ions compared to the pure epoxy coating. The EP-ABT/VN-MoN nanocomposite-coated mild steel exhibits a minimal intensity for Fe_2O_3 and γ-FeOOH. This results from the efficient bonding between the ABT and the VN-MoN nanocomposite via $-NH_2$ bond formation. Consequently, consistent dispersion of the coating led to the generation of fewer corrosion products. Moreover, the peaks of Fe_2O_3 and γ-FeOOH diminished in the primary and supplementary peaks observed for GO at 10.9° for the EP-GO/VN-MoN nanocomposite coated mild steel alloy. This confirms the effective interaction between GO and the VN/MoN nanoparticles, attributed to the epoxy, carboxyl, and hydroxyl groups, leading to the formation of uniform coatings inside the epoxy matrix. Consequently, the EP-GO/VN-MoN coatings exhibited a robust adhesion to the alloy, impeding the infiltration of corrosive ions through the coating. The EP-GO/ABT-VN/MoN nanocomposite-coated mild steel exhibited low-intensity peaks for Fe_2O_3 and γ-FeOOH.

In comparison to other polymer nanocomposite-coated mild steel alloys, the intensities of the supplementary peaks seen for GO, VN, and MoN were diminished and somewhat displaced. This verifies that effective covalent bond formation predominantly transpires between the VN and MoN nanoparticles via ABT functional groups through -NH- bonds. Furthermore, GO is firmly attached to the modified ABT via the hydroxyl group of GO and the secondary amine group of the ABT, leading to the creation of -N- bonds. The GO was connected to the modified ABT via this -NH- bond. The EP-GO/ABT-VN/MoN nanocomposite exhibited strong adhesion to the mild steel alloy surface owing to superior bond formation. The corrosion process was observed during prolonged immersion duration in the electrolyte of the nanocomposite-coated mild steel. The XRD study indicates that the EP-GO/ABT-VN/MoN nanocomposite serves as a protective barrier for mild steel alloys in comparison to other polymer nanocomposites.

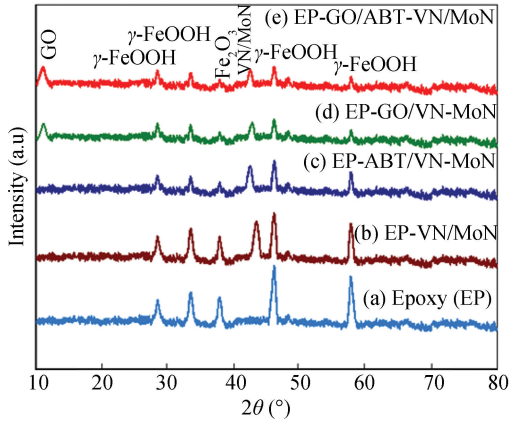

Fig. 9 XRD analysis of pure EP, EP-VN/MoN, EP-ABT/VN-MoN, EP-GO/VN-MoN, and EP-GO/ABT-VN/MoN nanocomposite coated steel after 45 d of immersion in 3.5% NaCl solution

2.4 Investigations of Surface Morphology

Following 45 d of immersion in the electrolyte, the morphologies of the studied coatings were examined using SEM, as illustrated in Fig.10. Fig.10 (a) illustrates that the coatings were inequitably distributed, exhibiting voids and cracks. This porous structure compromises the coating's adhesion to the substrate, allowing corrosive ions to penetrate easily. As a result, additional corrosion products are

generated[61]. In the EP-VN/MoN nanocomposites (Fig. 10 (b)), the VN and MoN nanoparticles obstruct the pre-existing pores in the epoxy covering. The hydrophilic characteristics of nanoparticles result in their aggregation on the epoxy coating. Consequently, partial pore coverage is evident, as illustrated in Fig. 10 (c), leading to a nonuniform distribution of the EP-VN/MoN nanocomposites on the coatings, which diminishes the mechanical characteristics at the interface between the coating and the steel. The EP-ABT/VN-MoN coating exhibits uniform dispersion on the mild steel alloy with minimal porosity. This is attributed to the effective functional interaction between ABT and VN/MoN through $-NH_2$ bonding. The nitrogen atom's lone pair of electrons was utilized to safeguard the surface of mild steel alloys from corrosion. Fig. 10 (e) illustrates that the nanocomposite generated fewer corrosion products owing to its uniform distribution across the mild steel alloy. Following 45 d of electrolyte exposure, the EP-GO/ABT-VN/MoN nanocomposite-coated mild steel alloy exhibited regulated corrosion resistance, verifying the successful bonding between GO and ABT modified VN/MoN nanocomposites via the amino group of ABT. Furthermore, GO established robust covalent connections with the epoxy matrix via the carboxyl group of GO. The successful functionalization resulted in a uniform dispersion of the nanocomposite on the surface of the mild steel alloy. Consequently, the EP-GO/ABT-VN/MoN nanocomposite serves as a protective barrier against the development of corrosion products, as illustrated in Fig.10. The coatings and the mild steel surface produce significant adhesive properties.

The EDX examination of the elemental composition of the investigated coated surface submerged in the electrolyte for 45 d is presented in Fig. 10. Fig.10(b) illustrates the presence of Fe, C, and O, thereby affirming the distribution of pure epoxy across the mild steel surface. The irregular distribution of high-density microvoid coatings may permit corrosive ions to infiltrate the metal surface. Moreover, a heightened peak for iron (predominantly in mild steel) signifies the existence of corrosive ions within the coating. It leads to the rapid formation of specific corrosion products. Fig.10(d) illustrates that the EP-VN/MoN nanocomposite coated mild steel alloy comprises carbon, nitrogen, oxygen, vanadium, molybdenum, and iron. The iron peak was significantly compressed relative to the pure epoxy coating. Subtle peak alterations were observed following the integration of VN/MoN nanoparticles into the epoxy matrix. Fig.10(f) illustrates the EP-ABT/VN-MoN nanocomposite applied to a mild steel alloy, consisting of carbon, sulfur, nitrogen, oxygen, iron, vanadium, and molybdenum. Furthermore, the peak seen for iron was diminished in comparison to EP and the EP-VN/MoN nanocomposite. This results from the efficient functionalization of VN-MoN nanoparticles with ABT via the main amino groups. This confirms the formation of a uniform coating and the decrease in corrosive ion infiltration. The efficiency of the EP-ABT/VN-MoN nanocomposite coating was enhanced. Fig.10(h) illustrates the chemical composition, including carbon, sulfur, nitrogen, oxygen, molybdenum, vanadium, and iron, in the mild steel alloy coated with the EP-GO/ABT-VN/MoN nanocomposite. Nevertheless, the peak achieved for iron was diminished in comparison to that of the other nanocomposites. This verifies the efficient distribution of the GO/ABT−VN/MoN nanocomposite within the epoxy covering. This is due to the efficient functionalization that transpires between GO and the ABT modified with the VN/MoN nanocomposites. The EP-GO/ABT-VN/MoN nanocomposite coating efficiently inhibited anion penetration into the metal surfaces for a prolonged duration. The mild steel alloy covered with the EP-GO/ABT-VN/MoN nanocomposite exhibited a uniform coating and exceptional protection with minimal dissolution.

2.5 Measurements of Water Contact Angle

Fig.11 illustrates the water contact angle (WCA) and static water droplet images of pure epoxy resin, EP-VN/MoN, EP-ABT/VN-MoN, and EP-GO/ABT-VN/MoN nanocomposite coated mild steel alloys. Hydrophilic surfaces exhibit a contact angle less than 90°. Hydrophobic surfaces exhibit contact angles between 90° and 150°. Surfaces exhibiting contact angles exceeding 150° are classified as superhydrophobic[62]. The pure epoxy-coated mild steel, with a water contact angle of 67°, is regarded as more hydrophilic. The epoxy was not equally disseminated, leading to the formation of small pores on the coated mild steel. Consequently, the absorption of water molecules transpires readily through these micropores, resulting in the water droplet manifesting as a semicircle in Fig.11(a). EP-VN/MoN demonstrates a water contact angle of 89°.

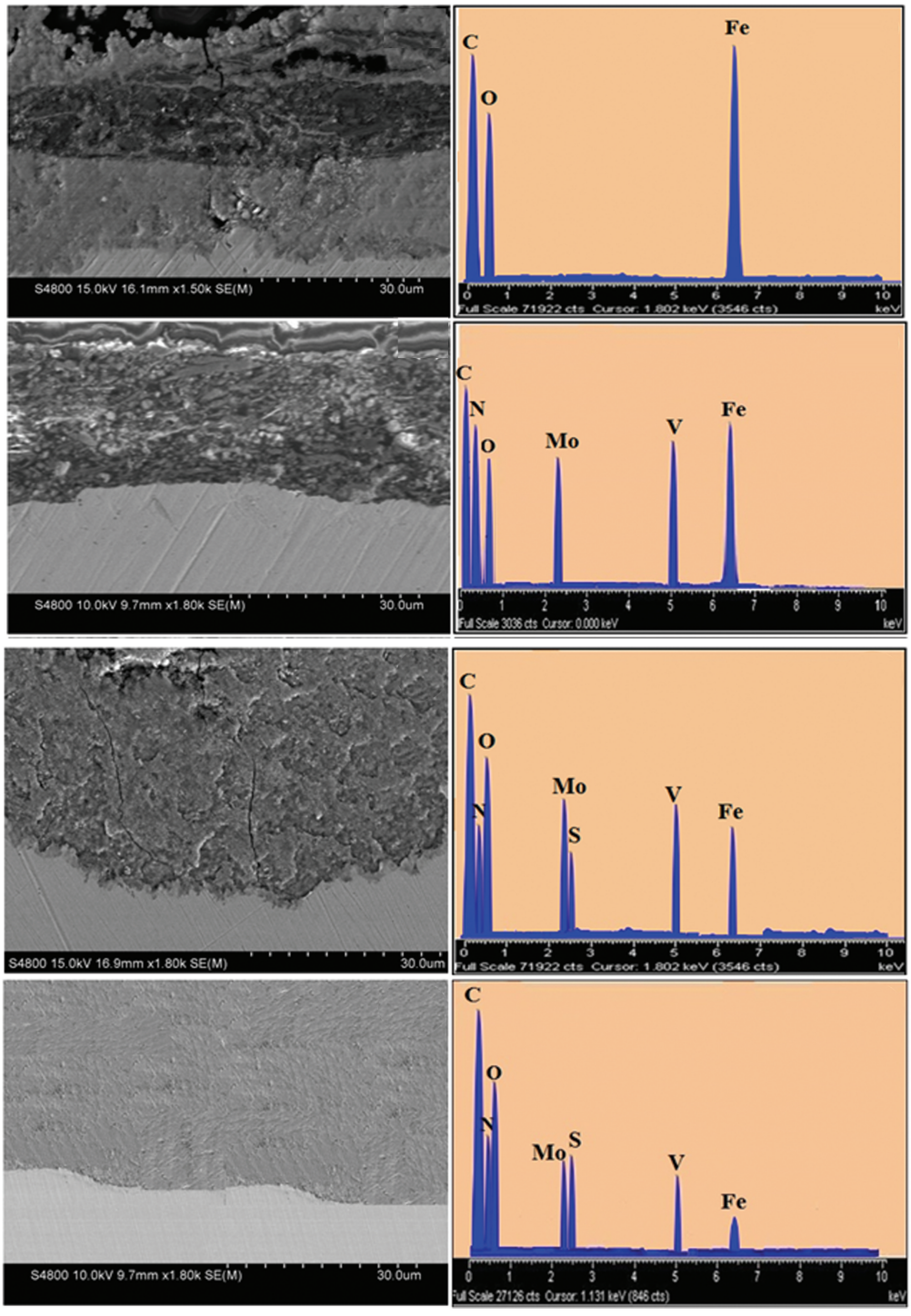

Fig.10 SEM/EDX (cross-sectional) analysis of EP (a & b), EP-VN/MoN (c & d), EP-ABT/VN-MoN (e & f), and EP-GO/ABT-VN/MoN (g & h) nanocomposite coated steel after 45 d of immersion in 3.5% NaCl solution

This demonstrates the hydrophilic characteristics of the coating resulting from the aggregation of VN/MoN particles. The EP-ABT/VN-MoN nanocomposite-coated mild steels exhibit water contact angles of 120°, categorizing them as hydrophobic. This pertains to the efficient functionalization of VN/MoN by the amino groups of ABT. Due to the functionalization of the nanoparticles, the adhesive strength of the nanocomposites to the mild steel alloy is enhanced, hence complicating the absorption of water molecules

on the coating. The EP-GO/ABT-VN/MoN nanocomposite coating achieves superhydrophobicity, evidenced by a high water contact angle of 159°. This remarkable performance is attributed to the synergistic effect of GO and ABT functional groups, which promote strong adhesion to the steel surface. Their presence ensures uniform nanoparticle dispersion within the epoxy matrix, significantly reducing agglomeration. As a result, the coating forms an effective barrier that prevents moisture ingress, inhibits water molecule penetration, and protects the alloy from oxidation and corrosion.

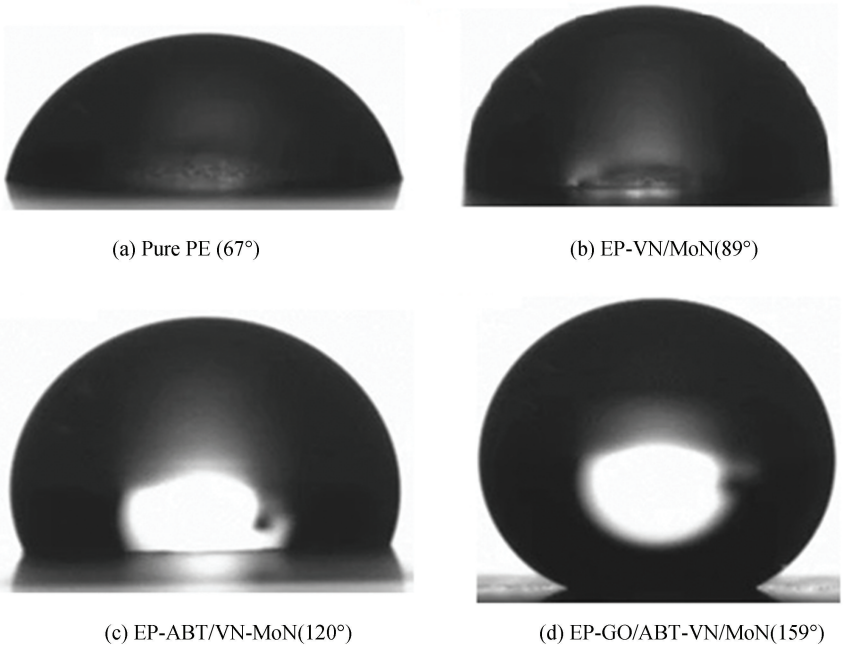

(a) Pure PE (67°) (b) EP-VN/MoN(89°)

(c) EP-ABT/VN-MoN(120°) (d) EP-GO/ABT-VN/MoN(159°)

Fig.11 Water contact angle measurements of pure EP, EP-VN/MoN, EP-ABT/VN-MoN, and EP-GO/ABT-VN/MoN nanocomposite

2.6 Mechanical Characteristics

Nanocomposite coatings, including pure epoxy, EP-VN/MoN, EP-ABT/VN/MoN, EP-GO/VN/MoN, and EP-GO/ABT-VN/MoN, were evaluated for adhesive strength Pre- and post-exposure to the electrolyte over various durations. The adhesive strength of pure epoxy coatings showed a significant decline, decreasing from 5.3 to 1.2 MPa after 45 d of immersion. This reduction is attributed to the presence of pores and weak adhesive bonds between the epoxy coating and the mild steel surface, allowing the negative ions in the NaCl solution to infiltrate the steel, resulting in the formation of corrosion products and a reduction in adhesion strength. The incorporation of VN/MoN nanoparticles into the epoxy matrix enhanced the adhesive strength. However, prolonged exposure led to some nanoparticle aggregation, limiting the improvement in adhesion strength, especially after 45 d of immersion. In this case, the gaps within the coating were not adequately filled, allowing corrosive ions to penetrate the mild steel surface. The adhesive strength of the EP-VN/MoN nanocomposite diminished slightly from 9.9 MPa after 1 d to 7.6 MPa after 45 d of immersion, consistent with the findings of epoxy-based coatings incorporating metal nitride nanoparticles. The EP-ABT/VN-MoN and EP-GO/VN-MoN nanocomposite coatings demonstrated superior adhesion strength, with values of 13.7 MPa and 15.8 MPa, respectively, after 1 d of exposure. After 45 d in the 3.5% NaCl solution, the adhesion strength decreased to 11.5 MPa and 15.0 MPa, respectively. The EP-GO/VN-MoN nanocomposite exhibited particularly strong adhesion due to the functionalization of VN/MoN with GO through various polyfunctional groups, including epoxy, carboxyl, and hydroxyl groups. These functional groups improved the interaction between GO and the epoxy matrix, ensuring an even distribution of the coating. As a result, the infiltration of ions into the mild steel surface was effectively hindered, leading to enhanced adhesion strength.

In comparison, the EP-GO/ABT-VN/MoN nanocomposite showed the most significant improvement in adhesion strength, increasing from 20.2 to 19.6 MPa after 1 d and 45 d in the electrolyte. This improvement can be attributed to the effective functionalization of GO with modified ABT using VN/MoN nanocomposites, which involved the amino groups of ABT. The non-bonding electrons in nitrogen effectively participate in the electrochemical process, mitigating corrosion of mild steel. This nanocomposite coating acts as a protective barrier against controlled corrosion, contributing to the significantly enhanced adhesion strength[63]. These findings underline the importance of incorporating functionalized nanocomposites, such as EP-GO/ABT-VN/MoN, in enhancing the long-term performance of protective coatings. These coatings demonstrate superior adhesion strength retention, even under challenging saline conditions, compared to pure epoxy coatings and other nanocomposites.

The mechanical properties, including hardness and tensile properties, of the nanocomposite-coated mild steel alloys were evaluated both before and throughout prolonged exposure to the electrolyte solution over several days. Table 3 indicates that the hardness and tensile properties of the epoxy-coated mild steel sample decreased from 1 d to 45 d. This illustrates that corrosion rapidly transpires via the pre-existing pores of the epoxy coating due to the interaction of negative ions in a 3.5% NaCl solution, hence diminishing the binding strength between the coating and the mild steel alloy surface. The hardness of the EP-VN/MoN nanocomposite decreased from 695 MPa at 1 day to 542 MPa after 45 d, while its tensile strength declined from 138 MPa to 99 MPa over the same period. The agglomeration of nanoparticles and the incomplete closure of existing fractures or pores in the epoxy coating led to nonuniform coatings on the mild steel surface. Ion penetration into the coating results in the formation of corrosion products. During immersion from 1 to 45 d in the electrolyte, the EP-ABT/VN-MoN and EP-GO/VN-MoN nanocomposites exhibited the least reduction in hardness and tensile strength. This verifies that a homogeneous dispersion of the coating was attained through the successful functionalization of amino groups via ABT interactions with the hydrophilic surface of the VN/MoN nanocomposite, as well as the interaction of GO with the VN/MoN nanocomposite through its oxygenated polyfunctional groups. The reduction in corrosion product formation contributed to improved mechanical performance of the nanocomposites, with hardness increasing from 891 to 1031 MPa and tensile strength rising from 166 to 181 MPa. The EP-GO/VN-MoN nanocomposite exhibited a more significant enhancement in mechanical strength than the EP-ABT/VN-MoN nanocomposite due to the presence of oxygenated polyfunctional groups in the GO.

In comparison to conventional nanocomposite coatings, the EP-GO/ABT-VN/MoN nanocomposite coating on mild steel alloy exhibited enhanced corrosion resistance and bonding strength during an extended immersion time of 45 d in a 3.5% NaCl solution. This results from the efficient functionalization between GO and the ABT modified with VN/MoN nanoparticles. Moreover, robust adhesion is seen between the epoxy and the functionalized graphene oxide nanocomposite. The nanocomposites were equally spread throughout the mild steel surface, enhancing the adhesion strength between the epoxy nanocomposite coating and the mild steel surface. This study revealed that the EP-GO/ABT-VN/MoN nanocomposite coating enhances the corrosion protection performance of steel by serving as a protective barrier.

2.7 Mechanism

Fig.12 illustrates the anti-corrosion mechanism exhibited by the nanocomposite coatings on mild steel alloys immersed in a 3.5% NaCl solution. The epoxy matrix is dense and cross-linked, serving as a protective barrier that inhibits the ingress of corrosive ions. Air entrapment and inadequate mixing during the curing process create pores in the epoxy coating. Corrosive ions in a 3.5% NaCl solution, including Cl^-, O_2, OH−, and SO_4^{2-}, can readily infiltrate the epoxy coating through the pre-existing pores. Corrosive chemicals generally infiltrate the coating/alloy interface, leading to the formation of hydroxyl ions in the cathodic areas through cathodic reduction and the liberation of ferrous ions (Fe^{2+}) from the anodic site by anodic oxidation of iron. The electrolyte (OH^-) reacts with ferrous ions, resulting in the formation of passive oxide layers. Simultaneously, ions in the electrolyte infiltrate the passive oxide layer via flaws at the coating/alloy contact, resulting in the formation of ferrous chloride. Ferrous chloride readily oxidizes from ferrous ions

(Fe^{2+}) to ferric ions (Fe^{3+}), hence expediting the corrosion process. Subsequently, the ferric ions react with H_2O and hydroxides, leading to the creation of FeOOH, Fe_2O_3, and Fe_3O_4[64].

Table 3 Mechanical properties of the nanocomposite films before and after immersion in several days in 3.5% NaCl solution

Coatings substrate	Exposure time(d)	Tensile strength (MPa)	Hardness (MPa)	Adhesion strength (MPa)
Epoxy resin (EP) coating	0	52±2	262±3	5.7±0.1
	1	50±2	239±2	5.3±0.3
	15	31±2	177±3	4.3±0.2
	30	22±1	97±2	2.8±0.1
	45	11±1	38±1	1.2±0.1
EP-VN/MoN coating	0	140±1	700±11	10.0±0.1
	1	138±3	695±12	9.9±0.2
	15	127±2	639±10	9.1±0.2
	30	111±2	590±11	8.3±0.1
	45	99±1	542±12	7.6±0.2
EP-ABT/VN-MoN coating	0	166±2	891±10	13.9±0.2
	1	162±1	882±11	13.7±0.2
	15	154±2	846±12	13.0±0.2
	30	145±1	824±10	12.2±0.1
	45	136±2	786±12	11.5±0.2
EP-GO/VN-MoN coating	0	181±1	1031±11	16.0±0.2
	1	179±2	1027±13	15.8±0.1
	15	173±1	1006±12	15.6±0.3
	30	165±2	986±11	15.1±0.1
	45	158±1	971±10	15.0±0.2
EP-GO/ABT/VN-MoN coating	0	256±2	1402±12	20.3±0.1
	1	255±1	1400±11	20.2±0.2
	15	252±1	1397±12	20.0±0.1
	30	248±2	1385±11	19.8±0.3
	45	244±1	1382±10	19.6±0.2

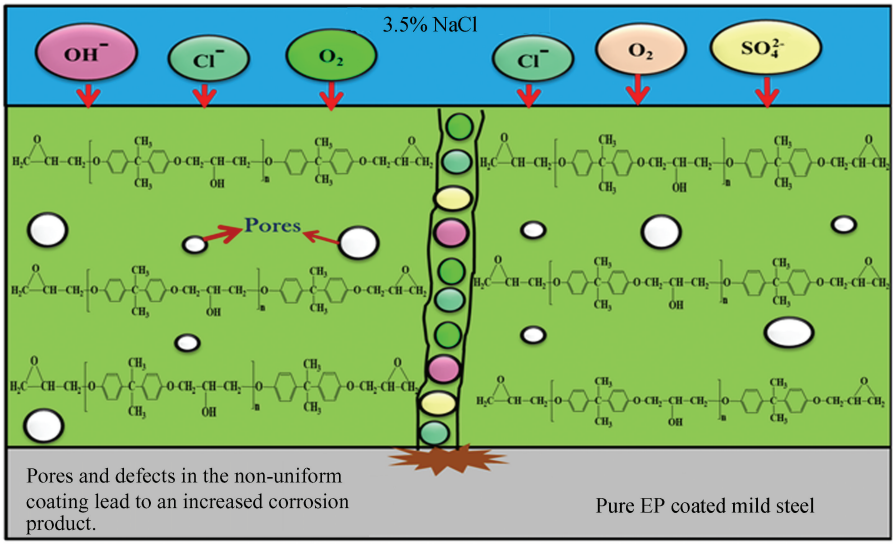

(a) Epoxy-coating

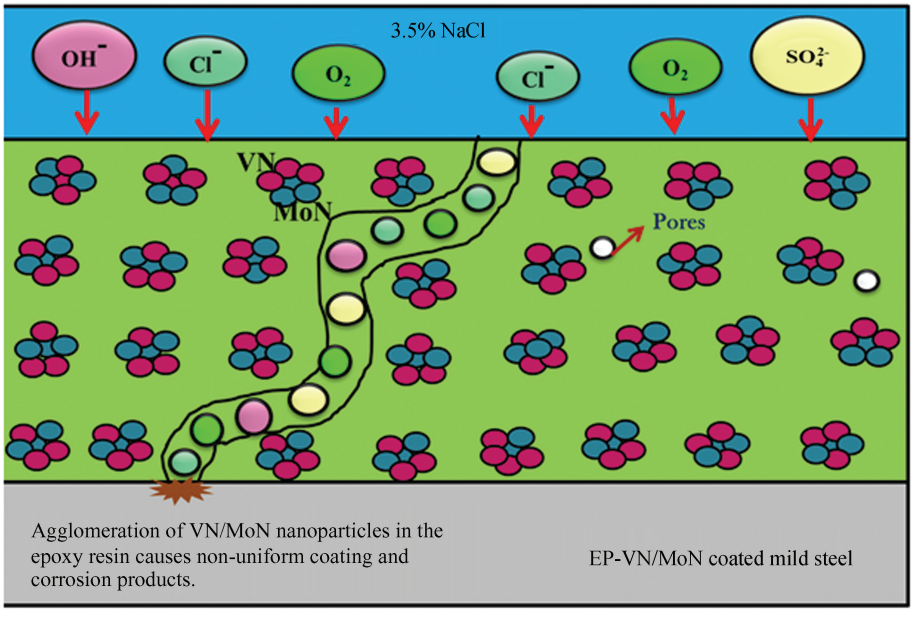

(b) EP-VN/MoN coating

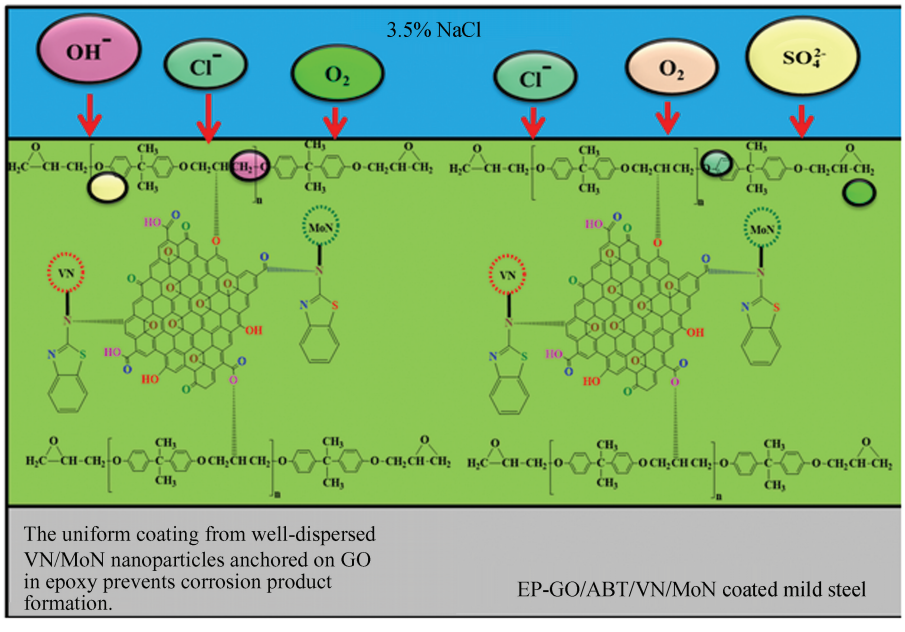

Fig.12 Protection mechanism of EP-GO/ABT-VN/MoN nanocomposite

The corrosion mechanism of mild steel alloys is explained as follows:

At anode (oxidation of Fe):

$$Fe \rightarrow Fe^{2+} + 2e^- \quad (2)$$

At cathode (reduction of O_2):

$$O_2 + H_2O + 4e^- \rightarrow 4OH^- \quad (3)$$

The corrosion reactions were as follows:

$$Fe^{2+} + 2Cl^- \rightarrow FeCl_2 \quad (4)$$

$$Fe^{2+} + H_2O \rightarrow FeOH^+ + H^+ \quad (5)$$

$$2FeOH^+ + O_2 + 2e^- \rightarrow 2\gamma\text{-}FeOOH \quad (6)$$

$$6FeOOH + 2e^- \rightarrow 2Fe_3O_4 + 2H_2O + OH^- \quad (7)$$

In comparison to the pure epoxy coating, the EP-VN/MoN nanocomposite coating on mild steel alloy offered superior corrosion protection at the interface. VN and MoN nanoparticles were included in the epoxy coating to enhance its physical barrier properties. These nanoparticles obstruct the micropores in the epoxy coating, leading to less corrosion deterioration. The corrosion process was partially regulated by the chemical interactions between the hydrophilic surfaces of the VN and MoN nanoparticles and the epoxy matrix. Nonetheless, nanoparticle aggregation results

in inadequate dispersibility of nano VN and MoN within epoxy resin. The EP-VN/MoN coating is irregular due to the formation of nanoparticle clusters on the coated alloy. The integration of ABT into the EP-VN/MoN nanocomposites diminishes nanoparticle agglomeration and facilitates even dispersion of VN/MoN within the coating. The amine group in ABT engages with the hydrophilic surface of VN and MoN nanoparticles, enhancing bonding strength and reducing nanoparticle aggregation. The lone pair of electrons on the nitrogen atom of the amine group may interact with the metal ions of the nanoparticle, leading to a more stable molecule. Consequently, the complex functions as a barrier, subtly limiting the interaction of corrosive ions with the coating. This transpired due to organic molecules with functional groups enhancing coordination with the nanoparticles, hence diminishing agglomeration and facilitating the formation of a uniform coating. Incorporating GO into the EP-VN/MoN nanocomposite strengthens the anti-corrosive efficiency and inhibits the ingress of aggressive ions into the coating. The EP/GO/VN/MoN nanocomposite coating exhibited superior charge resistance ($1.53\times10^{13}\ \Omega\cdot cm^2$) and coating resistance ($1.15\times10^{13}\ \Omega\cdot cm^2$) compared to the EP/ABT-VN/MoN coating, as determined by EIS analysis. This is due to the remarkable barrier properties of the graphene oxide layered structure, which is very impermeable and substantially diminishes ion incursion into the coating. The aggregation of VN and MoN nanoparticles is completely eliminated, leading to a uniform dispersion throughout the EP matrix. The layered structure of GO allows the EP matrix to encapsulate the metal surface fully. Consequently, prolonged immersion in the electrolyte allows the EP/GO/VN/MoN nanocomposite to protect the metal sample from detrimental ions and diminish corrosion products. The enhanced corrosion protection performance of the EP-GO/ABT-VN/MoN nanocomposite-coated mild steel alloys can be attributed to the synergistic effects of VN/MoN, GO, and ABT, culminating in a multifunctional coating that facilitates increased control over corrosion processes. The secondary amino groups in the VN and MoN nanoparticle-modified ABT chemically engage with the hydroxyl group of GO, leading to the formation of a very compact layered structure. A uniformly dispersed homogeneous covering including epoxy resin was achieved by robust hydrogen bonding interactions between modified graphene oxide and the ABT-VN/MoN nanocomposite and epoxy resin. The inclusion of GO and ABT alleviates the microgalvanic corrosion that may arise between the several layers of the coating. The augmented mechanical qualities conferred by ABT and GO boosted the coatings' resistance to scratches, abrasion, and impact, preserving their protective barrier even in severe conditions. The enhanced mechanical integrity of the coating guarantees prolonged endurance and diminished maintenance requirements. When applied to mild steel, the EP-GO/ABT-VN/MoN nanocomposite coating demonstrates exceptional stability and corrosion resistance, even after prolonged exposure to a 3.5% NaCl solution.

3 Conclusions

VN/MoN nanoparticles were functionalized with ABT, followed by the incorporation of GO to form ABT-modified nanocomposites. This hybrid system was designed to enhance both the anti-corrosion performance and mechanical strength of epoxy resin coatings. This study presents the first investigation of highly interactive modified VN/MoN nanoparticles integrated with GO and ABT within an epoxy (EP) resin matrix for enhanced anti-corrosion and mechanical performance. The functionalization of VN/MoN with ABT improved dispersion within the epoxy, while GO provided an effective barrier against corrosive agents. Electrochemical analysis demonstrated that the EP-GO/ABT-VN/MoN nanocomposite exhibited superior corrosion resistance, with the highest charge transfer resistance and lowest capacitance compared to pure EP and other nanocomposites. SECM analysis revealed reduced current distribution, indicating minimal iron oxide dissolution and prolonged corrosion protection in the electrolyte. Surface characterization (SEM, TEM, and EDX) proved the homogeneous dispersion of the nanocomposite, while XRD and XPS validated the structural and chemical modifications. Thermal analysis (TGA) demonstrated exceptional thermal stability of the nanocomposite due to strong covalent interactions. Mechanical testing revealed that the EP-GO/ABT-VN/MoN nanocomposite achieved the highest performance, with a bonding strength of 20.3 MPa, hardness of 1382 MPa, and superior tensile strength. These mechanical enhancements contribute to improved durability and corrosion protection of mild steel, thereby minimizing

material degradation and lowering maintenance costs. Consequently, this nanocomposite shows strong potential for industrial applications in marine, aerospace, and infrastructure sectors.

Supplementary Information

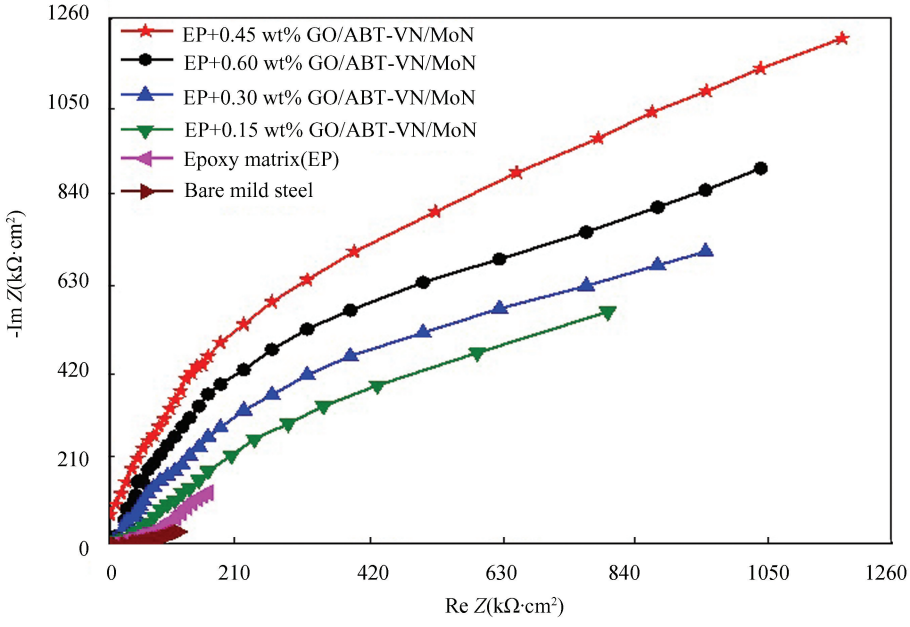

Fig. S1 Nyquist plots for epoxy coating with different weight percentages of GO/ABT-VN/MoN immersed in seawater for 1 d

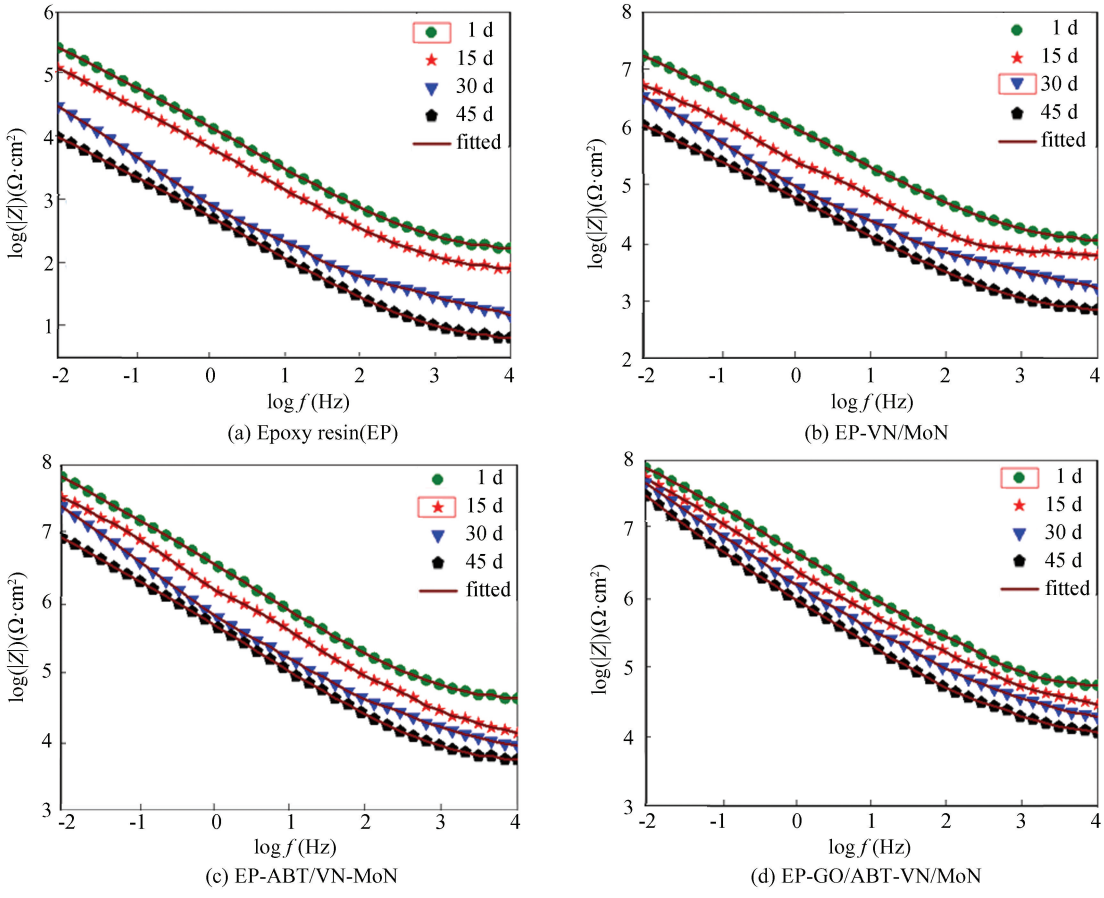

Fig. S2 Bode resistance plots for EP, EP-VN/MoN, EP-ABT/VN-MoN, and EP-GO/ABT-VN/MoN nanocomposite coated steel after 1, 15, 30, and 45 d of immersion in 3.5% NaCl solution

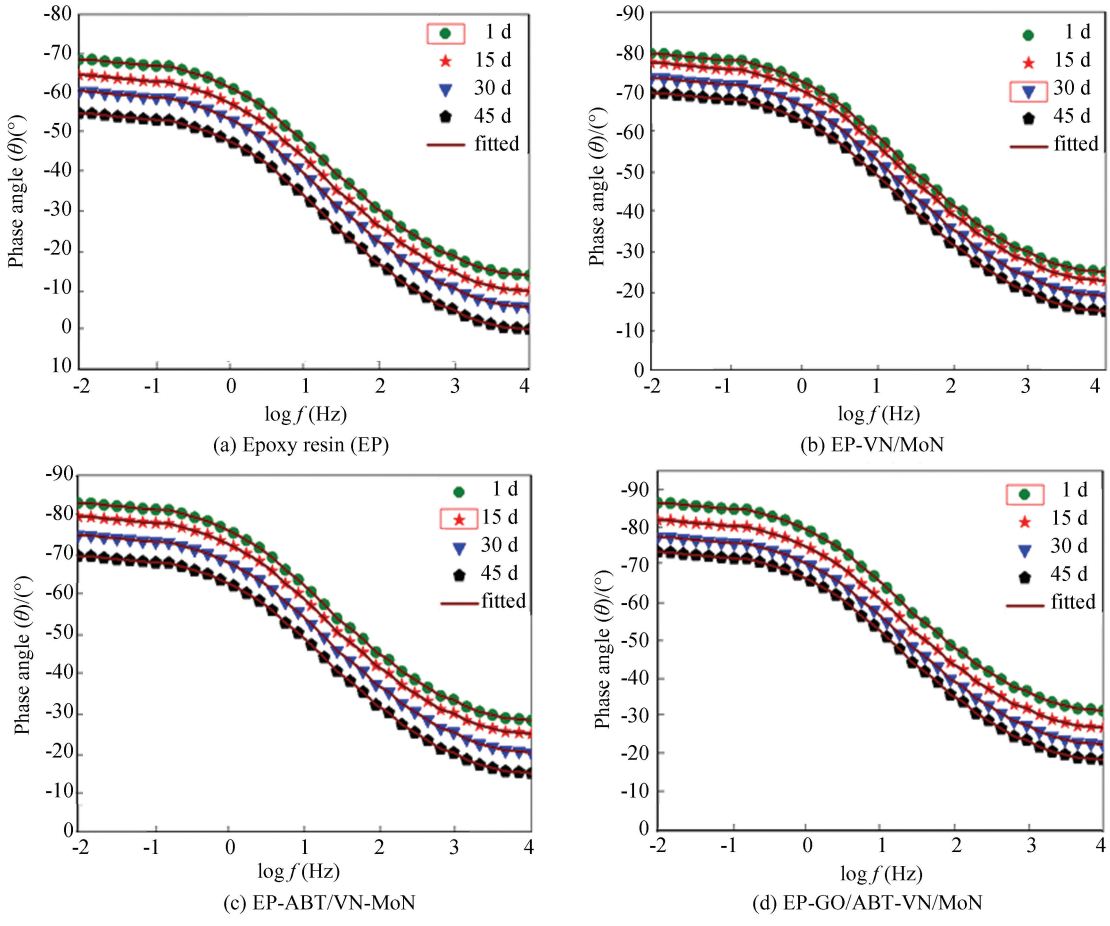

Fig. S3 Bode phase angle plots for EP, EP-VN/MoN, EP-ABT/VN-MoN, and EP-GO/ABT-VN/MoN nanocomposite coated steel after 1, 15, 30, and 45 d of immersion in 3.5% NaCl solution

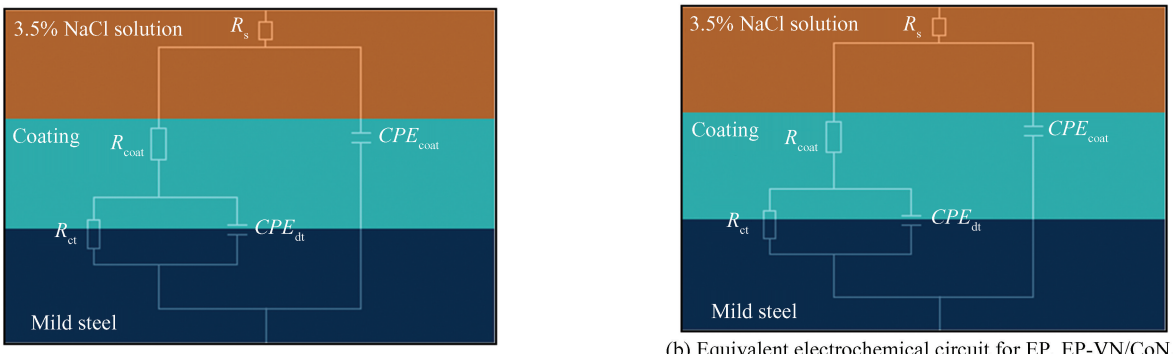

Fig. S4 Equivalent electrochemical circuit for bare mild steel, EP, EP-VN/CoN, EP-ABT/VN-MoN, and EP-GO/ABT/VN-MoN nanocomposite coated steel after 1, 15, 30, and 45 d of immersion in 3.5% NaCl solution

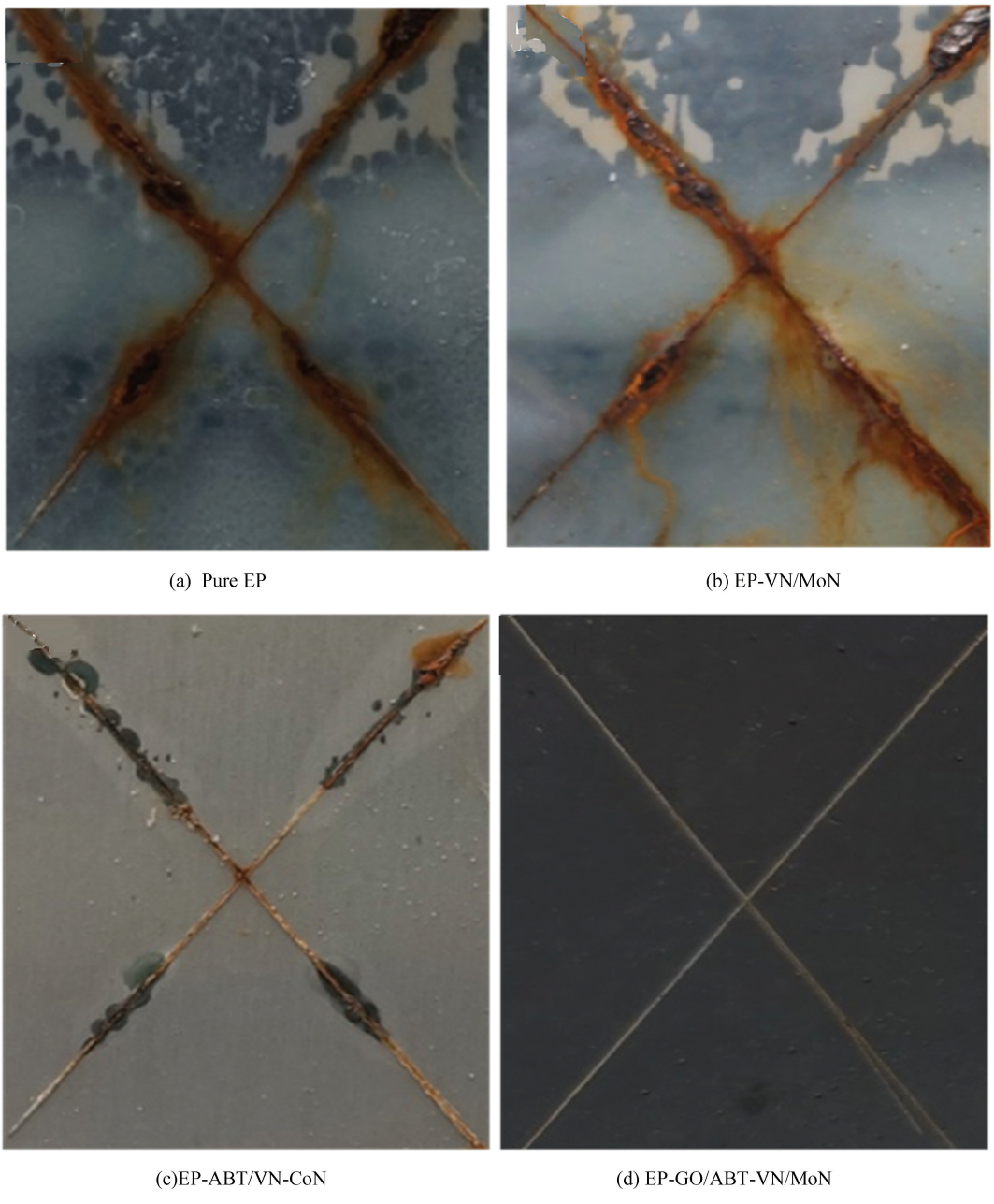

Fig. S5 Salt spray analysis of pure EP, EP-VN/MoN, EP-ABT/VN-CoN, and EP-GO/ABT-VN/MoN nanocomposite coated mild steel after 45 d exposure to 3.5% NaCl solution

References

[1] Wu X, Li J, Deng C, et al. Novel carbon dots as effective corrosion inhibitor for N80 steel in 1 M HCl and CO_2-saturated 3.5 wt% NaCl solutions. Journal of Molecular Structure, 2022, 1250: 131897. DOI: 10.1016/j.molstruc.2021.131897.

[2] Beryl J R, Xavier J R. A study on the anti-corrosion performance of epoxy nanocomposite coatings containing epoxy-silane treated nanoclay on mild steel in chloride environment. Journal of Polymer Research, 2021, 28: article number 189. DOI: 10.1007/s10965-021-02512-2.

[3] Xia Y Q, Zhang N G, Zhou Z P, et al. Incorporating SiO_2 functionalized g-C_3N_4 sheets to enhance anti-corrosion performance of waterborne epoxy. Progress in Organic Coatings, 2020, 147: 105768. DOI: 10.1016/j.porgcoat.2020.105768.

[4] Perumal G, Deepanraj B, Senthilkumar N, et al. Mechanical characterization and enhancing wear properties of Glass/Sisal/nAl_2O_3 strengthened polymer matrix nanocomposites using hybrid optimization approach. Results in Engineering, 2025, 26: 104568. DOI: 10.1016/j.rineng.2025.104568.

[5] Elangovan N, Srinivasan A, Pugalmani S, et al. Development and electrochemical investigations of enhanced corrosion - resistant Polyvinylcarbazole-TiO_2 hybrid nanocomposite coatings on 316L SS for marine applications. Surface and Coatings Technology, 2024, 481: 130628. DOI: 10.1016/j.surfcoat.2024.130628.

[6] Khamme E, Sakulkalavek A, Sakdanuphab R. Anti-corrosion performance of vinyl ester resin films with titanium dioxide and graphene hybrid reinforcement. Materials Today Communications, 2022, 33: 104888. DOI: 10.1016/j.mtcomm.2022.104888.

[7] Vinodhini S P, Xavier J R. Effect of graphene oxide wrapped functional silicon carbide on structural, surface protection, water repellent, and mechanical properties of epoxy matrix for automotive structural components. Colloids and Surfaces A: Physicochemical and Engineering Aspects, 2022, 639: 128300. DOI: 10.1016/j.colsurfa.2022.128300.

[8] Raja Beryl J, Xavier J R. Investigation into the effects of silanized nanoclay on the barrier properties of epoxy resin in chloride environment. Journal of Molecular Structure, 2022, 1264: 133264. DOI: 10.1016/j.molstruc.2022.133264.

[9] Varshney S, Chugh K, Mhaske S T. Effect of layer-by-layer synthesized graphene-polyaniline-based nanocontainers for corrosion protection of mild steel. Journal of Materials Science, 2022, 57: 8348 - 8366. DOI: 10.1007/s10853-022-07208-6.

[10] He Z, Lin H, Zhang X, et al. Self-healing epoxy composite coating based on polypyrrole @ MOF nanoparticles for the long-efficiency corrosion protection on steels. Colloids and Surfaces A: Physicochemical and Engineering Aspects, 2023, 657 (Part A): 130601. DOI: 10.1016/j.colsurfa.2022.130601.

[11] Kabeb S M, Hassan A, Ahmad F, et al. Synergistic effects of hybrid nanofillers on graphene oxide reinforced epoxy coating on corrosion resistance and fire retardancy. Journal of Applied Polymer Science, 2022, 139 (7): 51640. DOI: 10.1002/app.51640.

[12] Xavier J R. Novel multilayer epoxy nanocomposite coatings for superior hydrophobic, mechanical and corrosion protection properties of steel. Diamond and Related Materials, 2022, 123: 108882. DOI: 10.1016/j.diamond.2022.108882.

[13] Habib S, Fayyad E, Nawaz M, et al. Cerium dioxide nanoparticles as smart carriers for self-healing coatings. Nanomaterials, 2020, 10 (4): 791. DOI: 10.3390/nano10040791.

[14] Xavier J R. Investigation on the effect of nano-ceria on the epoxy coatings for corrosion protection of mild steel in natural seawater. Anti-Corrosion Methods and Materials, 2018, 65 (1): 38-45. DOI: 10.1108/ACMM-04-2017-1784.

[15] Nguyen-Tri P, Nguyen T A, Carriere P, et al. Nanocomposite coatings: preparation, characterization, properties, and applications. International Journal of Corrosion, 2018, 2018: Article ID 4749501. DOI: 10.1155/2018/4749501.

[16] Xavier J R, Nallaiyan R. Application of EIS and SECM studies for investigation of anti-corrosion properties of epoxy coatings containing ZrO_2 nanoparticles on mild steel in 3.5% NaCl solution. Journal of Failure Analysis and Prevention, 2016, 16: 1082 - 1091. DOI: 10.1007/s11668-016-0187-x.

[17] El Sayed M Y, Abdel-Gaber A M, Rahal H T. Safranin—A potential corrosion inhibitor for mild steel in acidic media: a combined experimental and theoretical approach. Journal of Failure Analysis and Prevention, 2019, 19: 1174 - 1180. DOI: 10.1007/s11668 - 019 - 00719-6.

[18] Lu F, Liu C, Chen Z, et al. Polypyrrole-functionalized boron nitride nanosheets for high-performance anti-corrosion composite coating. Surface & Coatings Technology, 2021, 420: 127273. DOI: 10.1016/j.surfcoat.2021.127273.

[19] Wang H, Qi Q, Zhang Y, et al. Anticorrosive epoxy nanocomposite coatings filled with polyaniline-functionalized silicon nitride particles. Industrial & Engineering Chemistry Research, 2020, 59 (38): 16649-16659. DOI: 10.1021/acs.iecr.0c02460.

[20] Kiahosseini S R, Afshar A, Mojtahedzadeh Larijani M, et al. Structural and corrosion characterization of hydroxyapatite/zirconium nitride-coated AZ91 magnesium alloy by ion beam sputtering. Applied Surface Science, 2017, 401: 172-780. DOI: 10.1016/j.apsusc.2017.01.022.

[21] Padmanabhan V P, Pugalmani S, Veerla S C, et al. An alternative approach in the synthesis of strontium-hydroxyapatite and strontium hydroxyapatite embedded in graphitic carbon nitride nanocomposites for potential tissue engineering applications. Diamond and Related Materials, 2024, 149: 111561. DOI: 10.1016/j.diamond.2024.111561.

[22] Situ Y, Ji W, Liu C, et al. Synergistic effect of homogeneously dispersed PANI-TiN nanocomposites towards long-term anticorrosive performance of epoxy coatings. Progress in Organic Coatings, 2019, 130: 158-167. DOI: 10.1016/j.porgcoat.2019.01.034.

[23] Rajeshwari P, Dey T K. Novel HDPE nanocomposites containing aluminum nitride (nano) particles: micro-structural and nano-mechanical properties correlation. Materials Chemistry and Physics, 2017, 190: 175 - 186. DOI: 10.1016/j.matchemphys.2017.01.020.

[24] Lule Z, Kim J. Surface modification of aluminum nitride to fabricate thermally conductive poly (butylene succinate) nanocomposite. Polymers, 2019, 11 (1): 148. DOI: 10.3390/polym11010148.

[25] Kim K, Ju H, Kim J. Pyrolysis behavior of polysilazane and polysilazane-coated boron nitride for high thermal

conductive composite. Composites Science and Technology, 2017,141:1-7. DOI:10.1016/j.compscitech.2017.01.003.

[26] Huanbo H, Yansheng Z, Yushi D, et al. Preparation of polyaniline/nano SiC/epoxy hybrid coating and evaluation of its corrosion resistant property. Journal of Polymer Materials, 2016,33:1-15.

[27] Jeeva N, Thirunavukkarasu K, Xavier J R. Influence of multifunctional graphene oxide and silanized vanadium nitride in polyurethane coatings for the protection of aluminium alloy in aerospace industries. Diamond and Related Materials, 2024, 142: 110792. DOI: 10.1016/j.diamond.2024.110792.

[28] Fan D, Liu X, Qi K, et al. A smart-sensing coating based on dual-emission fluorescent Zr-MOF composite for autonomous warning of coating damage and aluminum corrosion. Progress in Organic Coatings, 2022, 172: 107150, DOI:10.1016/j.porgcoat.2022.107150.

[29] Li X, Chen X, Chen J, et al. Development of an epoxy resin-based anticorrosive coating enhanced by monolayer amino-modified graphene oxide. Progress in Organic Coatings, 2024, 194: 108624, DOI: 10.1016/j.porgcoat.2024.108624.

[30] Xavier J R, Vinodhini S P. Investigation of newly synthesized environmentally friendly graphene oxide multilayer nanocoating for enhancing the protection performance of steel structure. Journal of Industrial and Engineering Chemistry, 2022, 115: 147-161. DOI: 10.1016/j.jiec.2022.07.046.

[31] Ou Z, Kong G, Zhang J, et al. Preparation and anti-corrosion performance of graphene-reinforced epoxy powder coating. Journal of Materials Research and Technology, 2024,28:4626-4638. DOI:10.1016/j.jmrt.2024.01.086.

[32] Wu Y, He Y, Chen C, et al. Non-covalently functionalized boron nitride by graphene oxide for anticorrosive reinforcement of water-borne epoxy coating. Colloids and Surfaces A: Physicochemical and Engineering Aspects,2020,587:124337. DOI:10.1016/j.colsurfa.2019.124337.

[33] Vinodhini S P, Xavier J R. Evaluation of newly synthesized multifunctional nanocomposite coated cupronickel alloy in marine environment. Materials Chemistry and Physics, 2021, 268: 124721. DOI: 10.1016/j.matchemphys.2021.124721.

[34] Vinodhini S P, Xavier J R, Priyadharshini A. A review on flame retardant, anti-corrosion, and mechanical properties of multifunctional polymer nanocomposite coatings for industrial applications. Progress in Organic Coatings, 2025, 206: 109361. DOI: 10.1016/j.porgcoat.2025.109361.

[35] Bordbar-Khiabani A, Ebrahimi S, Yarmand B. Highly corrosion protection properties of plasma electrolytic oxidized titanium using rGO nanosheets. Applied Surface Science, 2019, 486: 153-165. DOI: 10.1016/j.apsusc.2019.05.026.

[36] Ebrahimi S, Bordbar-Khiabani A, Yarmand B. Immobilization of rGO/ZnO hybrid composites on the Zn substrate for enhanced photocatalytic activity and corrosion stability. Journal of Alloys and Compounds, 2020,845:156219. DOI:10.1016/j.jallcom.2020.156219.

[37] Compton O C, Nguyen S T. Graphene oxide, highly reduced graphene oxide, and graphene: versatile building blocks for carbon-based materials. Small, 2010, 6(6): 711-723. DOI:10.1002/smll.200901934.

[38] Wang M-H, Li Q, Li X, et al. Effect of oxygen-containing functional groups in epoxy/reduced graphene oxide composite coatings on corrosion protection and antimicrobial properties. Applied Surface Science, 2018, 448:351-361. DOI:10.1016/j.apsusc.2018.04.141.

[39] Steffi A P, Balaji R, Chandrasekar N, et al. High-performance anti-corrosive coatings based on rGO-SiO_2-TiO_2 ternary heterojunction nanocomposites for superior protection for mild steel specimens. Diamond and Related Materials, 2022, 125: 108968. DOI: 10.1016/j.diamond.2022.108968.

[40] Boomadevi Janaki G, Xavier J R. Effect of indole functionalized nano-alumina on the corrosion protection performance of epoxy coatings in marine environment. Journal of Macromolecular Science, 2020, 57(10): 691-702. DOI:10.1080/10601325.2020.1761831.

[41] Abazari S, Shamsipur A, Bakhsheshi-Rad H R, et al. Graphene family nanomaterial reinforced magnesium-based matrix composites for biomedical application: A comprehensive review. Metals, 2020, 10(8): 1002. DOI: 10.3390/met10081002.

[42] Huang M, Yang J. Salt spray and EIS studies on HDI microcapsule-based self-healing anticorrosive coatings. Progress in Organic Coatings, 2014, 77(1): 168-175. DOI:10.1016/j.porgcoat.2013.09.002.

[43] Arianpouya N, Shishesaz M, Arianpouya M, et al. Evaluation of synergistic effect of nanozinc/nanoclay additives on the corrosion performance of zinc-rich polyurethane nanocomposite coatings using electrochemical properties and salt spray testing. Surface & Coatings Technology, 2013, 216(1): 199-206. DOI: 10.1016/j.surfcoat.2012.11.036.

[44] Kezuka Y, Tajika M. Fracture strength evaluation of agglomerates of fatty acid-coated $CaCO_3$ nanoparticles by nano-indentation. ChemEngineering, 2019, 3(3): 73. DOI:10.3390/chemengineering3030073.

[45] Dubey R, Dutta D, Sarkar A, et al. Functionalized carbon nanotubes: synthesis, properties and applications in water purification, drug delivery, and material and biomedical sciences. Nanoscale Advances, 2021, 3(22): 5722-5744. DOI:10.1039/D1NA00293G.

[46] Cui X F, Qiao Y J, Liu R L, et al. Effects of current density on the corrosion behaviour of anodized aluminum alloy in $FeCl_3$ solution. Journal of Harbin Institute of

Technology (New Series), 2012, 19(3): 56-60. DOI: 10.11916/j.issn.1005-9113.2012.03.010.

[47] Lin B, Xu Y, Lu J. Self-healing behavior of phosphate coating post-sealed with molybdate. Journal of Harbin Institute of Technology (New Series), 2017, 24(4): 90-96. DOI: 10.11916/j.issn.1005-9113.15306.

[48] Xavier J R. Novel multifunctional epoxy based graphitic carbon nitride/silanized TiO_2 nanocomposite as protective coatings for steel surface against corrosion and flame in the shipping industry. Journal of Central South University, 2024, 31(10): 3394-3422. DOI: 10.1007/s11771-024-5788-z.

[49] Xavier J R. Electrochemical and dynamic mechanical studies of newly synthesized polyurethane/SiO_2-Al_2O_3 mixed oxide nanocomposite coated steel immersed in 3.5% NaCl solution. Surfaces and Interfaces, 2021, 22: 100848. DOI: 10.1016/j.surfin.2020.100848.

[50] Xavier J R. Investigation on the anti-corrosion, adhesion and mechanical performance of epoxy nanocomposite coatings containing epoxy-silane treated nano-MoO_3 on mild steel. Journal of Adhesion Science and Technology, 2019, 34(2): 115-134. DOI: 10.1080/01694243.2019.1661658.

[51] Xavier J R, Jeeva N. Evaluation of newly synthesized nanocomposites containing thiazole modified aluminium nitride nanoparticles for aerospace applications. Materials Chemistry and Physics, 2022, 286: 126200. DOI: 10.1016/j.matchemphys.2022.126200.

[52] Wu Y, He Y, Chen C, et al. Non-covalently functionalized boron nitride by graphene oxide for anticorrosive reinforcement of water-borne epoxy coating. Colloids and Surfaces A: Physicochemical and Engineering Aspects, 2019, 587: 124337. DOI: 10.1016/j.colsurfa.2019.124337.

[53] Xia Y, Zhang N, Zhou Z, et al. Incorporating SiO_2 functionalized g-C_3N_4 sheets to enhance anti-corrosion performance of waterborne epoxy. Progress in Organic Coatings, 2020, 147: 105768. DOI: 10.1016/j.porgcoat.2020.105768.

[54] Nayak S R, Mohana K N S. Corrosion protection performance of functionalized graphene oxide nanocomposite coating on mild steel. Surfaces and Interfaces, 2018, 11: 63-73. DOI: 10.1016/j.surfin.2018.03.002.

[55] Vinodhini S P, Xavier J R. Investigation of anti-corrosion and mechanical properties of azole functionalized graphene oxide encapsulated epoxy coatings on mild steel. Journal of Failure Analysis and Prevention, 2021, 21(2): 649-661. DOI: 10.1007/s11668-020-01104-4.

[56] Fazli-Shokouhi S, Nasirpouri F, Khatamian M. Polyaniline-modified graphene oxide nanocomposites in epoxy coatings for enhancing the anti-corrosion and antifouling properties. Journal of Coatings Technology and Research, 2019, 16: 983-997. DOI: 10.1007/s11998-018-00173-3.

[57] Tabish M, Zhao J, Kumar A, et al. Developing epoxy-based anti-corrosion functional nanocomposite coating with CaFe-Tolyl-triazole layered double hydroxide @ g-C_3N_4 as nanofillers on Q235 steel substrate against NaCl corrosive environment. Chemical Engineering Journal, 2022, 450 (Part 1): 137624. DOI: 10.1016/j.cej.2022.137624.

[58] Liu J, Yu Q, Yu M, et al. Silane modification of titanium dioxide-decorated graphene oxide nanocomposite for enhancing anti-corrosion performance of epoxy coatings on AA-2024. Journal of Alloys and Compounds, 2018, 744: 728-739. DOI: 10.1016/j.jallcom.2018.01.267.

[59] Vinodhini S P, Xavier J R. Novel multifunctional nanocomposites containing graphitic carbon nitride/silanized Nb_2O_5 nanofillers for the protection of steel surfaces in the automobile industry. Journal of Molecular Structure, 2024, 1306: 137875. DOI: 10.1016/j.molstruc.2024.137875.

[60] Xavier J R, Vinodhini S P, Raja Beryl J. Flame retardant and corrosion protection performance of multifunctional nanocomposites containing graphitic carbon nitride/silanized Ta_2O_2 nanofillers for the protection of steel surface for industrial applications. Colloids and Surfaces A: Physicochemical and Engineering Aspects, 2024, 681: 132748. DOI: 10.1016/j.colsurfa.2023.132748.

[61] Ma A L, Jiang S L, Zheng Y G, et al. Corrosion product film formed on the 90/10 copper-nickel tube in natural seawater: composition/structure and formation mechanism. Corrosion Science, 2015, 91: 245-261. DOI: 10.1016/j.corsci.2014.11.028.

[62] Ammar S, Ramesh K, Ma I A W, et al. Studies on SiO_2-hybrid polymeric nanocomposite coatings with superior corrosion protection and hydrophobicity. Surface & Coatings Technology, 2017, 324: 536-545. DOI: 10.1016/j.surfcoat.2017.06.014.

[63] Kang W, Zhang L, Li M. Graphene oxide and polyfunctional groups-based hybrid nanocomposites for enhancing adhesion and corrosion protection in coatings. Journal of Materials Research and Technology, 2022, 23: 1502-1512.

[64] Zhang H, Yan L, Zhu Y, et al. The effect of immersion corrosion time on electrochemical corrosion behavior and the corrosion mechanism of EH47 ship steel in seawater. Metals, 2021, 11(8): 1317. DOI: 10.3390/met11081317.